M 2018

U.PORTO
FEUP FACULDADE DE ENGENHARIA
UNIVERSIDADE DO PORTO

PREPARATION OF CARBON-BASED ELECTRODES TO BE USED AS BACK-CONTACT IN PEROVSKITE SOLAR CELLS

ANA CRISTINA ORNELAS TEIXEIRA

DISSERTAÇÃO DE MESTRADO APRESENTADA
À FACULDADE DE ENGENHARIA DA UNIVERSIDADE DO PORTO EM
ENGENHARIA QUÍMICA

Master in Chemical Engineering

Preparation of carbon-based electrodes to be used as back-contact in perovskite solar cells

A Master's dissertation

of

Ana Cristina Ornelas Teixeira

Developed within the course of dissertation

held in

LEPABE

Supervisor at FEUP: **Doctor Luísa Andrade**

Co-Supervisor: **Professor Adélio Mendes**

Departamento de Engenharia Química

july of 2018

Acknowledgment

Firstly, I would like to thank my supervisor Doctor Luísa Andrade for the enormous support she has always given to me since the beginning of the thesis. I am very grateful for the opportunity to participate in a project in an area that I have always wanted to work on, for all the time and patience with me trying to solve all the problems that appeared, for the constant presence in all stages of the thesis and for making sure that I always had everything I needed to get the best results possible.

I must also thank my co-supervisor, Professor Adélio Mendes, for giving me the opportunity to do this dissertation within Solar Group in a laboratory with such privileged working conditions and for always being willing to help and give advice about my work.

This work was partially supported by the European Union's Horizon 2020 programme, through a FET Open research and innovation action under Project GOTSolar (grant agreement No 687008) and by the Projects "SunStorage - Harvesting and storage of solar energy", funded by European Regional Development Fund (ERDF), through COMPETE 2020 - Operational Programme for Competitiveness and Internationalisation (OPCI), and by national funds, through FCT - Fundação para a Ciência e a Tecnologia I.P. and POCI-01-0145-FEDER-006939 - Laboratory for Process Engineering, Environment, Biotechnology and Energy – LEPABE and NORTE-01-0145-FEDER-000005 – LEPABE-2-ECO-INNOVATION, funded by FEDER funds through COMPETE2020 - Programa Operacional Competitividade e Internacionalização (POCI) and Programa Operacional Regional do Norte (NORTE2020) and by national funds through FCT - Fundação para a Ciência e a Tecnologia.

I would also like to thank to Rita Arnaldo for all the transmitted knowledge about PSC and her support, especially at the beginning. To Isabel Mesquita, Mafalda Pereira, Carlos Almeida, Daniela Aguiar and Carolina Eiras Sá I would like to thank you for the guidance, friendship and all the help you gave me every time I needed. I am also very grateful to Vera Duarte, Mariana Donato, Gabriel Bernardo and Margarida Catarino for providing me with materials for my work, and to the other members of the Solar Group and researchers from LEPABE, for receiving me so well and for always being so readily helpful in any situation.

I cannot forget thanking all my friends from my course and from TUNAFE, who made these 5 years the best years of my life, for all the good times we spent together, for giving me support in the harder ones and for making me a happier person. A special thanks to Moisés, André and Joana Lopes for the lunch time company and Joana Martins for being my 24/7 companion.

I must also give my heartfelt thanks to my flatmates, Ana, Catarina, Paula, Rita and Slávia, who have accompanied me closely since the beginning, for all the motivation, kind words and emotional support, especially in the in times of increased anxiety.

Last but not least, my biggest thanks is to my parents, Celina and Carlos, and my sister Xana tótó, for being always there in every time of my life, for all the motivation and support, even if from very far, and for giving me the opportunity to take this course.

Abstract

Renewable energy sources provide an excellent opportunity for the reduction of greenhouse gas emissions and the mitigation of global warming through replacing conventional energy sources such as fossil fuels. Solar energy is the most abundant renewable source, with 1.8×10^{14} kW of irradiance being intercepted by earth, and many studies are being developed in order to collect the solar radiation and efficiently convert it to electrical energy for supply, with reduced energy loss and lower production costs. Direct solar energy conversion into electricity is done using photovoltaic cells. Perovskite solar cells (PSC) are an emerging photovoltaic technology with a great potential to revolutionize the photovoltaic field with a very rapid growth from 3.8 % power conversion efficiency to 23.3 % in just 9 years. PSCs present low-cost and easy fabrication processes, compatibility with flexible plastic substrates for large-area production and special features for building-integrated photovoltaics, like transparency and different possibilities of color. However, there are still limitations hindering its commercialization, as the expensive and highly thermally unstable back-contact made of gold. A possible alternative is a carbon-based back-contact, whose features, such as abundant sources, high electrical conductivity, chemical stability, diversity, modifiability and suitable work function, makes it ideal for replacing the currently used gold. Indeed, in this work the main goal is to replace the expensive gold back-contact. Two different approaches were followed: i) use of opaque carbon papers aiming for low-cost PSC devices; ii) preparation of a graphene-based back-contact by thermal chemical vapor deposition aiming for semitransparency.

Carbons papers are designed for proton-exchange membrane fuel cells; this thesis presents a pioneer work using carbon papers as back-contact in solar cells. In this approach, different adhesion layers (spiroOMeTAD and PEDOT:PSS) were tested to enhance the interfacial contact between the carbon paper and the hole transport material of the perovskite solar cell and two different carbon papers were studied to perceive the influence of the paper characteristics. A maximum power conversion efficiency of 6.91 % was reached with the best configuration; there was a loss of 1 % in the fill factor and an increase of 4 % in the open-circuit voltage for the best-performing cells when compared with gold reference device.

Regarding the study of the graphene growth, the selected synthesis technique was chemical vapor deposition because it allows the synthesis of large area graphene, with high uniformity and low defects, and enables the exploitation of a wide variety of transition metals as catalysts. The critical point of controlling the oxidation of the copper surface at high temperatures was assessed. This oxidized surface is responsible for the lack of graphene growth since Cu catalyzes the reaction and, if oxidized, methane cannot decompose into graphene layers. An effective

purge process is then necessary before starting the CVD process in order to eliminate the oxidizing impurities inside the tube. The catalyst (copper) deposition on a silicon wafer by sputtering was performed and all CVD variables were deeply studied and optimized to synthesize multilayer graphene, due to its lower sheet resistance when compared with few-layer graphene.

Keywords: Perovskite Solar Cells, Back-contact, Carbon papers, Graphene, Chemical vapor deposition

Resumo

As fontes de energia renováveis contribuem para a redução das emissões de gases de efeito estufa e a mitigação do aquecimento global por substituírem as fontes de energia convencionais como os combustíveis fósseis. A energia solar é a fonte renovável mais abundante, com 1.8×10^{14} kW de irradiância a ser intercetada pela Terra, e sendo muitos estudos desenvolvidos no intuito de captar a radiação solar e convertê-la eficientemente em energia elétrica para fornecimento, minimizando as perdas de energia e os custos de produção. A conversão direta de energia solar em eletricidade é conseguida através de células fotovoltaicas. As células solares de perovskita (PSC) são uma tecnologia fotovoltaica emergente, com grande potencial para revolucionar o campo fotovoltaico, devido ao rápido crescimento da sua eficiência de conversão de energia de 3,8 % até 22,7 % em apenas 8 anos. As PSCs apresentam processos de fabricação simples e de baixo custo, compatibilidade com substratos plásticos flexíveis para produção em grande escala e recursos especiais para sistemas fotovoltaicos integrados em edifícios, como transparência e diferentes possibilidades de cor. No entanto, ainda existem limitações que dificultam a sua comercialização, como o contra-elétrodo caro e termicamente instável feito de ouro. Uma alternativa possível para o contra-elétrodo são materiais de carbono, que apresentam fontes abundantes, alta condutividade elétrica, estabilidade química, diversidade, modificabilidade e função de trabalho adequada, o que os tornam na alternativa ideal para a substituição do ouro atualmente usado. De facto, neste trabalho o objetivo principal é substituir o contra-elétrodo de ouro dispendioso. Duas abordagens diferentes foram seguidas: i) uso de papéis de carbono opacos visando dispositivos PSC de baixo custo; ii) preparação de um contra-elétrodo baseado em grafeno por deposição química de fase vapor visando a semitransparência.

Os papéis de carbonos são projetados para células de combustível de membrana de troca de protões; esta tese apresenta um trabalho pioneiro na utilização de papéis de carbono como contra-elétrodo em células solares. Nesta abordagem, diferentes camadas de adesão (SpiroOMeTAD e PEDOT:PSS) foram testadas para melhorar o contacto na interface entre o papel carbono e o material transportador de lacunas da célula solar de perovskita e dois diferentes tipos papéis de carbono foram estudados para perceber a influência das suas características. Foi alcançada uma eficiência máxima de conversão de energia de 6,91% com a melhor configuração; houve uma perda de 1% no fator de preenchimento e um aumento de 4% no potencial de circuito aberto para as células com melhor desempenho quando comparado com o dispositivo de referência de ouro.

No que diz respeito ao estudo da produção do grafeno, a técnica de síntese selecionada foi a deposição química em fase vapor, pois permite a síntese de grafeno em grande escala, com alta uniformidade e baixos defeitos, e possibilita a exploração de uma grande variedade de

metais de transição como catalisadores. Foi avaliado o controlo da oxidação da superfície do cobre a altas temperaturas. Esta superfície oxidada é responsável pela inibição do crescimento de grafeno, uma vez que o cobre catalisa a reação e, se oxidar, o metano não se decompõe em camadas de grafeno. É então necessário um processo de purga eficaz antes de iniciar o processo de CVD para eliminar as impurezas oxidantes dentro do tubo. A deposição de catalisador (cobre) num disco de silício foi realizada por *sputtering* e todas as variáveis de CVD foram profundamente estudadas e otimizadas para sintetizar grafeno multicamada, devido à sua menor resistência de folha quando comparado com o grafeno de poucas camadas.

Palavras-chave: Células solares de Perovskita, contra-elétrodo, papéis de carbono, grafeno, deposição química em fase vapor

Declaration

I hereby declare, on my word of honour, that this work is original and that all non-original contributions were properly referenced with source identification.

Index

List of Figures

List of Tables

Notation and Glossary

FF	Fill factor	
V_{oc}	Open circuit voltage	V
I_{sc}	Short circuit current	$mA \cdot cm^{-2}$
V	Voltage	V
I	Current	A
η	Efficiency	

List of Acronyms

PSC	Perovskite solar cell
PCE	Power conversion efficiency
HTM	Hole transporting material
CNT	Carbon nanotube
PEMFC	Proton-exchange membrane fuel cells
PCVD	Plasma enhanced chemical vapor deposition
CVD	Thermal chemical vapor deposition
LEPABE	Laboratory for Process Engineering, Environment, Biotechnology and Energy
MA	Methylammonium
FA	Formamidinium
Cs	Cesium
DSC	Dye-sensitized solar cell
TCO	Transparent conductive oxide
TiO_2	Titanium dioxide
Au	Gold
Ag	Silver
GDL	Gas Diffusion Layer
SiO_2/Si	Silicon dioxide on silicon
MG	Multilayer graphene
PEDOT:PSS	Poly-(3,4-ethylenedioxythiophene): poly(styrenesulfonate)
Ni	Nickel
Cu	Copper
Ar	Argon
H_2	Hydrogen

GB	Glove Box
XRD	X-Ray Diffraction
FLG	Few-layer graphene
SEM	Scanning electron microscopy
AFM	Atomic force microscopy
SKPM	Scanning Kelvin probe microscopy
PDMS	Polydimethylsiloxane
I-V	Photocurrent-voltage

1 Introduction

1.1 Framing and presentation of the work

Over the past years, energy needs have been increasing intensively, not only due to industrial sector growth, but also due to world population increase. Currently, the main source of energy is fossil fuels, providing more than 80 % of the world's energy, and despite being very accessible, easy to transport, reliable and cheap, it leads to a significant adverse impact on the environment, such as global warming and climate changes. [1, 2] To overcome these issues, serious efforts are being made in order to make energy production more sustainable and environmentally friendly, bearing in mind costs, reliability, convenience, efficiency and other critical factors. Solar energy is the most abundant renewable source, with 1.8×10^{14} kW of irradiance being intercepted by earth, and many studies are underway in order to collect the solar radiation and efficiently convert it to electrical energy for supply, with reduced energy losses and lower production costs. [2]

Solar cells technologies are divided into three generations according to the materials they are made of. The first one is based on silicon solar cells, which are the most common. The second generation comprehends the thin film solar cells as amorphous silicon (a-Si), Copper indium gallium selenide (CIGS) and Cadmium telluride (CdTe) and finally the third generation covers solar cells made of organic materials, such as small molecules or polymers, and also expensive high performance experimental multi-junction solar cells. Typical power conversion efficiency (PCE) ranges for each solar cell technology are presented in Table 1.1. [3, 4]

Table 1.1 - Typical power conversion efficiencies ranges for each solar cell technology. [4]

Solar cell technology	Silicon	a-Si, CIGS and CdTe	Organic	Multi-junction
Efficiency range	20 % - 30 %	15 % - 25 %	10 % - 20 %	25 % - 45 %

PCE corresponds to the percentage of solar energy irradiated onto the panel that is effectively converted into electric energy. A new class of thin film solar cells that recently emerged in the photovoltaic field is the perovskite solar cells (PSCs). These cells show a huge potential due to their rapid PCE improvement from 3.8 % in 2009 up to 23.3 % in 2018, which is comparable to the commercial silicon solar cells. Furthermore, PSCs present a low-cost and easy fabrication process, compatibility with flexible plastic substrates for large-area production and special features for building-integrated photovoltaics like transparency and different possibilities of color. [5] However, there are still barriers hindering its commercialization, like its instability in the presence of moisture and oxygen, some high energy-consumption fabrication processes (such as gold evaporation and mesoporous layer annealing), harsh requirement for production

facilities and the high cost of the typical hole-transporting-material (HTM) and noble metallic back-contact (usually gold). In addition to the high cost, the back-contact has other limitations such as the diffusion of gold atoms into the perovskite's layer at high temperatures and silver corroding when in contact with perovskite, resulting in dramatic loss of device performance under working conditions. To overcome these problems, many studies are considering using carbon materials as back contact, such as carbon pastes (mixture of graphite and carbon black), carbon nanotubes (CNTs) and graphene. [6]

A carbon material that has not been yet tested for solar cell applications is carbon paper. This material is specifically used for proton-exchange membrane fuel cells (PEMFC), being its structure and morphology designed according to the requirements of behaving as a gas diffusion layer. However, its high conductivity, suitable work function, high mechanical and chemical stability and low cost makes it a potential substitute for the gold counter-electrode.

On the other hand, graphene, known as being a very versatile material, has proven to be a good candidate to replace the typical noble metals used as counter electrode due to its topping mobility, absorbance, conductivity, mechanical flexibility, transparency, specific surface area and low cost production when compared to gold and silver. [6] Graphene can be synthetized through different methods including mechanical exfoliation and cleavage, chemical synthesis, thermal decomposition of silicon carbide (SiC), un-zipping CNTs, plasma enhanced chemical vapor deposition (PCVD) and thermal chemical vapor deposition (CVD), the latter being the most promising because it has confirmed reproducibility of high-quality graphene on a large scale. However, it still presents some challenges, such as controlling the number of layers and minimizing folds and wrinkles. [7]

In this work, the main goal is to replace the expensive and thermally unstable gold back-contact. Carbon materials can be used as a cost effective back-contact with satisfactory energy efficiency performances. Two different approaches will be studied: i) use of opaque carbon papers aiming for low-cost PSC devices; ii) preparation of a graphene-based back-contact by thermal CVD aiming for semitransparency.

1.2 Presentation of the laboratory

The present work was developed in the Laboratory for Process Engineering, Environment, Biotechnology and Energy (LEPABE). LEPABE was created in 1997, as an interdisciplinary group, to operate within FEUP - Chemical Engineering Department. It is the largest research unit operating within FEUP in the fields of Chemical, Environmental and Biological Engineering. LEPABE has been consistently classified as "Excellent" by the various international evaluation panels appointed by the Science and Technology Foundation (FCT) and from 2008 to 2017 the

number of researchers increased from 98 to 170, most of which doctorate researchers (from 29 to 73).

LEPABE's mission is to develop innovative processes and products to respond effectively to society challenges, accelerating significant improvement in the wealth and well-being of European society. The consistency of the unit stems from the common matrix - analysis of chemical and biological systems - applied to the development of innovative processes and products with high economic potential, integrating energy, environment and safety issues. Synergies resulting from the complementary research groups surely contribute to the sustainable socio-economical and industrial development of the country.

To support this mission, LEPABE is structured into 3 research groups: (a) Chemical Processes Engineering and Energy, (b) Biotechnology and Interfaces and (c) Environment, which cross-feed with 5 thematic lines that are our research priorities: (1) Processes, Products and Energy; (2) Process Systems Engineering; (3) Biotechnology; (4) Supramolecular Assemblies and (5) Environmental Sciences and Technologies. This work was developed within research line Processes, Products and Energy. [8]

1.3 Contributions of the Work

The main contribution of my work concerning graphene production, was the determination of the limitations and optimization of the procedures for the use of the laboratory's tubular furnace in the production of multilayer graphene, namely the cleaning procedure, the determination of the significant variables and the most adequate range values for them, and the evaluation of copper deposited by two different sputtering equipments. Then, all the CVD experiments described within the thesis, as well as modifications in the experimental setup, were performed by me. Additionally, all morphological characterization techniques, even if subcontracted to an external laboratory, were performed under my accompaniment. The deposition of copper by sputtering was not performed by me.

Considering the carbon papers work, all the experimental work was performed by me: optimization of the adhesion layers deposition, integration of carbon papers into full devices, assembling of complete PSC devices and photovoltaic performance characterization. Important to mention that the procedure for assembling efficient reference PSC devices with ≈16 % was already optimized in the host laboratory. The study I have done on carbon papers is at the forefront of the use of carbon papers as back-contact for PSCs. The conclusions I drew from this study may open doors for a new area of applications for this material and the results obtained showed that there is still a great opportunity to improve the material itself as to better satisfy the requirements of a good back-contact.

1.4 Organization of the thesis

The present thesis is organized in 6 chapters:

1st chapter – Introduction – The topic of research within this thesis is contextualized and the main objectives are presented. The host laboratory is presented and the author's contribution to the work is clearly stated.

2nd chapter – Context and State of the art – This chapter envisages to give the state of the art concerning the technology under study, and so working principles, device architectures and overall challenges of perovskite solar cells are highlighted. Then, after framing the objectives of the thesis, a detailed review concerning PSC's back-contact limitations and respective carbon alternatives are presented.

3rd chapter – Materials and Methods – The materials used as well as the experimental procedures performed are described: PSC assembly, carbon paper preparation and assembly on the PSC, graphene synthesis by chemical vapor deposition. Characterization techniques are also presented: Raman spectroscopy, XRD, SEM, AFM, SKPM and solar cell performance evaluation.

4th chapter – Results and discussion – This thesis is divided in two main studies: use of carbon papers as back-contact for PSCs and growth of graphene by chemical vapor deposition. The most relevant results obtained within the two studies are presented and discussed. Carbon paper discussion focuses on the use of different adhesion layers and carbon papers and consequent photovoltaic performance under complete PSC devices, while the graphene synthesis discussion focuses on the effect of operating conditions, the design of experiments for optimizing the CVD process and the definition of cleaning procedures to avoid oxidation of the metallic catalysts.

5th chapter – Conclusions – Main conclusions drawn from the discussion of results as well as the most important results are presented.

6th chapter – Assessment of the work done – A retrospective analysis of the work performed is carried out, in which the fully reached objectives are stated and it is explained why the initially forecasted results were not achieved. This leads to identification of the main limitations that occurred during the prosecution of the work and future work suggestions.

2 Context and State of the art

2.1. Perovskite solar cells

Organic–inorganic hybrid lead halide perovskites have been studied since the 70s due to their unique semiconductive and conductive properties. [9] Perovskite, named after the Russian mineralogist L.A. Perovski, has a specific crystal structure with the generic ABX_3 formula, where A, B and X refer to a large organic cation, a large inorganic cation, and a slightly smaller anion, respectively. [10]

For use in solar cells, cation A is generally either a methylammonium (MA), formamidinium (FA), cesium (Cs), rubidium (Rb) cation or a combination of them, cation B is usually lead (Pb) or tin (Sn) and anion X is usually a halogen (predominantly iodine (I), bromine (Br) and chlorine (Cl) also being of interest), but it could also be oxygen, carbon or nitrogen. [11, 12] The larger A cation occupies a cube-octahedral site shared with twelve X anions, while the smaller B cation is stabilized in an octahedral site shared with six X anions - Figure 2.1. [12]

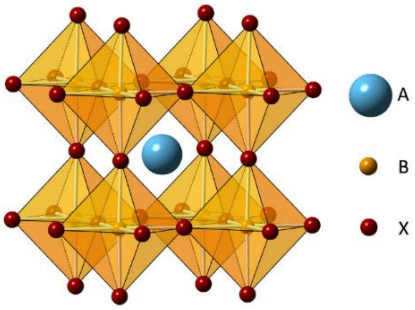

Figure 2.1 - Perovskite structure. [21]

The anions/cations combination to form the perovskite structure is chosen based on its geometric tolerance factor t defined as $t = (r_A + r_X)/[\sqrt{2}(r_B + r_X)]$, where r_A, r_B and r_X are the effective ionic radius for A, B and X ions, respectively. [13] Besides being synthesized from abundant sources (inorganic and organic perovskite compounds), perovskites can have an impressive array of interesting properties depending on which atoms/molecules are used in the structure, including superconductivity, high magnetoresistance, large charge carrier mobility, high absorption coefficient, spin-dependent transport (spintronics) and catalytic properties. [10, 14]

Perovskite was applied to solar cells for the first time in 2009 by Miyasaka et al. [14] They used two types of perovskites as visible-light sensitizers in photovoltaic cells, achieving a PCE of 3.8 % and 3.1 %. [14] Since then, perovskite architecture, deposition processes and composition have been modified in order to enhance its PCE with recent devices reaching 23.3 % (in July 2018 at CAS – Chinese Academy of Science). This makes the perovskite solar cells the technology with the fastest performance evolution within the photovoltaic field. Furthermore, the record efficiency of 23.3 % surpassed the efficiency of multi-crystalline silicon (22.3 %), CIGS (22.9 %) and CdTe (22.1 %) solar cells, and are getting very close to the efficiency of single-crystalline silicon cells (26.1 %). [4] Solar cell efficiency improvement throughout the years until 2018 is

presented in Appendix 1. In addition to the high values of efficiency, some of the perovskite solar cells fabrication methods are low-cost (e.g. spray pyrolysis and spin coating) and their photoactive layers present high absorbance, allowing the utilization of ultrathin films, which also reduce the costs. [10, 15] Perovskite films can also be color-tuned into bright and colorful displays, which shows its potential for building integrated photovoltaics. [16] Thus, these features make it possible to manufacture high-efficient, thin, lightweight, flexible and eye-pleasing solar cells. Despite these notable features, PSCs are poorly stable under ambient conditions for long periods of time, not fulfilling the market requirements. Stability is one of the biggest concerns being studied but Arora et al. [17] already managed to produce PSCs that retain more than 95 % of their initial efficiency after being aged at maximum power point for 1000 hours under full solar intensity at 60 °C. [17]

2.1.1 Working principles

PSCs are a stem of dye-sensitized solar cells (DSCs) since both share similar operational mechanisms. The most conventional PSC architecture is the mesoporous configuration and it is composed by five layers - Figure 2.2 (a):

1) Glass substrate with one surface coated with a transparent conductive oxide (TCO) - this layer acts as photoelectrode and allows the sunlight to pass through so its transmittance needs to be high. While glass protects the perovskite solar cells from the adverse weather conditions, the TCO coating is responsible for conducting the excited electrons from the blocking layer to the external circuit.

2) Compact semiconductor (blocking layer) – this layer is made of a n-type material, usually titanium dioxide (TiO_2) and its function is to extract electrons inhibiting holes to cross. [12] It also prevents the direct contact between the transparent conductive oxide and hole transporting material, hindering short circuits.

3) Mesoporous semiconductor film - this layer acts as a scaffold for the electrons to flow, capturing the photoinjected electrons from the perovskite and conducting them to the blocking layer. [18]

4) Perovskite Layer – is the photoactive layer, absorbing photons from visible spectrum to near-infrared. When the perovskite absorbs a photon, an electron-hole pair is created. Electrons are then driven to the n-i junction while holes are driven to the i-p junction, creating thereby a planar-junction diode, which is responsible for the charges separation. Thus, perovskite not only works as light absorber but also as an ambipolar electron and hole transporter. During deposition, perovskite solution infiltrates the pores of the semiconductor scaffold and the excess solution forms a “capping layer” on top of the filled mesoporous oxide,

which prevents the mesoporous layer from contacting directly with the HTM and, consequently, prevents short circuits. [18, 19]

5) Hole transport material (HTM) – composed by a p-type material, this layer has the function of "pulling" holes from the perovskite and conducting them through a hopping mechanism to the back-contact. Its main requirements are: high hole mobility, an optimal HOMO energy level, good film forming properties, and low cost, being 2,2',7,7'-Tetrakis[N,N-di(4-methoxyphenyl)amino]-9,9'-spirobifluorene ($C_{81}H_{68}N_4O_8$), known as spiroOMeTAD, the most commonly used.

6) Electrical conductive back-contact – usually thermally evaporated gold (Au). This is the final layer and it connects to the external circuit, receiving electrons from the photoelectrode. These electrons recombine with the holes from the HTM in the interface HTM/back-contact. [18] It should be made of a very conductive and stable material in order to enhance charge flow.

For typical solar cells (single-junction) the maximum PCE possible to attain is about 30 %, denominated the theoretical Shockley–Queisser limit, which is calculated by the amount of electrical energy that is extracted per photon of incoming sunlight. Thus, the PCE is directly related with the bandgap and fermi levels of the different components, as well as some certain degrading and sunlight incidence geometrical factors, such as materials absorption coefficient of the solar energy radiation and the radiation incidence angle. [20] Band gap is the energy between the valence and conduction band potential, while fermi levels are the energy require to send an electron to vacuum, this is, to ionize the atom. Thereby, these fermi levels are one of the biggest concerns when choosing suitable components for the PSC since they have to ensure charge flow through the different components with minimal energy loss. The conventional methyl ammonium lead iodide ($MAPbI_3$) perovskite presents a band gap of about 1.55 eV (HOMO level ≈-3.9 eV and LUMO level ≈-5.4 eV), which guarantees a large absorption coefficient in the visible range, and therefore a good PCE - Figure 2.2(b). [21]

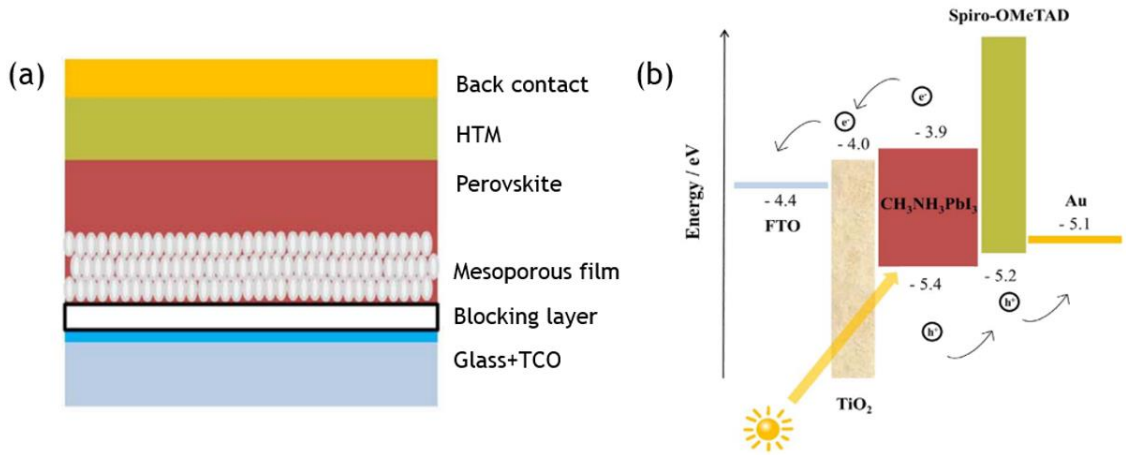

Figure 2.2 - (a) Illustrative scheme of a typical mesoporous PSC. (b) Energy diagram and main processes occurring in a PSC: photons absorption, free charge generation and charge transport through the different layers (adapted from Mesquita et al.). [18]

2.1.2 Device architectures

Different device architectures have been studied in order to improve PSC performance, stability and scalability, showing that notable efficiencies are not confined to a single architecture. This high versatility may be justified by the excellent optoelectronic properties of the perovskite class of materials. [22] Nevertheless, stability is very dependent on device architecture, mainly because of the presence or absence of some critical layers, such as HTM. [23]

PSC architectures can be divided into five configurations:

1) Mesoporous conductive semiconductor PSC – this is the most studied and it was already described above.

2) Mesoporous insulating PSC – the conductive scaffold material is replaced by an insulator one, whose function is to provide surface area for the perovskite settling, being electrons transmitted through the perovskite material.

3) Planar PSC – The mesoporous material is removed and perovskite contacts directly with the blocking layer. This configuration is interesting because it eliminates problems related with the infiltration of perovskite material in the scaffold pores and its fabrication is simpler, being more scalable.

4) HTM-less PSC – Similar to planar but without HTM layer. In this attempt the HTM stability does not compromise the whole cell stability, but the perovskite thickness and uniformity is crucial to avoid shunt pathways (in case of contact between the blocking layer and the back-contact).

5) Inverted PSC – the HTM and blocking layer change places, being that the electrons flow in the reverse direction. [18]

The highest PCE values reached by these different architectures and the respective year are presented in the Table 2.1.

Table 2.1 – Record PCE values for the different PSC architectures.

Architecture	Mesoporous conductive semiconductor [4]	Mesoporous insulating [24]	Planar [25]	HTM-less [26]	Inverted [27]
Maximum PCE	23.3 %	15.9 %	20.9 %	13.5 %	19.9 %
Year	2018	2014	2016	2018	2017

2.1.3 Overall challenges

Besides the great efficiency results of the different PSC architectures, there are still technological limitations hindering their commercial relevance, mainly concerning stability and cost-effectiveness. Regarding stability, the main barriers are: degradation in the presence of moisture, oxygen and temperature; photoinduced phase segregation in mixed-cation mixed-halide perovskites; photoinduced dissociation of organic cations; and migration of gold atoms across the HTM layer, from the counter-electrode to the perovskite material. [28] The ultimate goal in PSCs stability research is to accomplish long device lifetime, and so different approaches are being developed to prevent water, air and high energy photons from getting into the device. Among these approaches are the application of barrier layers directly onto perovskites and devices, the introduction of stable electrodes, and proper device encapsulation. [29] On costs, the main barriers are: high cost of the typical HTM materials and noble metallic counter-electrodes; high energy-consumption of certain fabrication processes (e.g. gold deposition by evaporation and high sintering temperatures for the mesoporous layer); and harsh requirement for production facilities. [6, 23] Low-cost but also more thermally stable substitutes for spiroOMeTAD are being studied, with inorganic (CuI and CuSCN) and polymeric HTMs (PTAA and P3HT) becoming possible alternatives. For noble metallic counter-electrodes the best choice are carbon materials. [18]

The presence of lead is also a topic of concern due to its toxicity to humans. However, these cations are fundamental to stabilize the perovskite structure, change the lattice constant, define the band gap and determine the electronic structure of perovskite. Other cations are being tested to replace lead, tin being the most suitable candidate, although it is more expensive and toxic to the environment than lead and has poor chemical stability. Other candidates for replacing lead are mixed cations structures lead-tin, bismuth and other metal cations from the IIA, IV and V groups. [18, 29] In fact, the lead-tin composition is the favored approach for reducing the lead-content and, at the same time, allow reaching the adequate quality of the perovskite material. [30]

2.2 Perovskite Back-Contact

2.2.1 Limitations

As mentioned before, counter-electrodes (i.e. back-contact) currently being used have several limitations not only related with thermal and chemical stability but also with price and transparency. It has been confirmed that the back-contact that allows the highest PCE is Au, due to its suitable fermi level and very high conductivity. However, Au is one of the most expensive metals (and the most expensive material in PSC) and also needs production techniques that require high vacuum and high temperature, consuming large amounts of energy and consequently increased fabrication costs. [6]

Furthermore, if heated above 70 °C, which is easily achievable in a hot and sunny day, gold atoms may migrate through the HTM layer to the perovskite film - Figure 2.3. This can produce shunts across the device and trap states within the semiconductor, which enhances non-radiative recombination. [23] Consequently, open circuit voltage (V_{oc}) values decrease significantly, which results in a severe loss in PCE. Domanski et al. [23] measured the amount of Au in a sample aged at 70 °C, confirming the presence of 72.8 ng of Au (in the control sample the amount of Au was below the detection limit of the instrument that was ~1 ng for the amount of solution used). [23] Thereby, removing gold from PSC composition would significantly reduce the price of the cell's fabrication, enhance its stability that is one of the biggest concerns of this solar cell technology, reduce the energy requirement, and increase device transparency making it possible to light the cell from both sides.

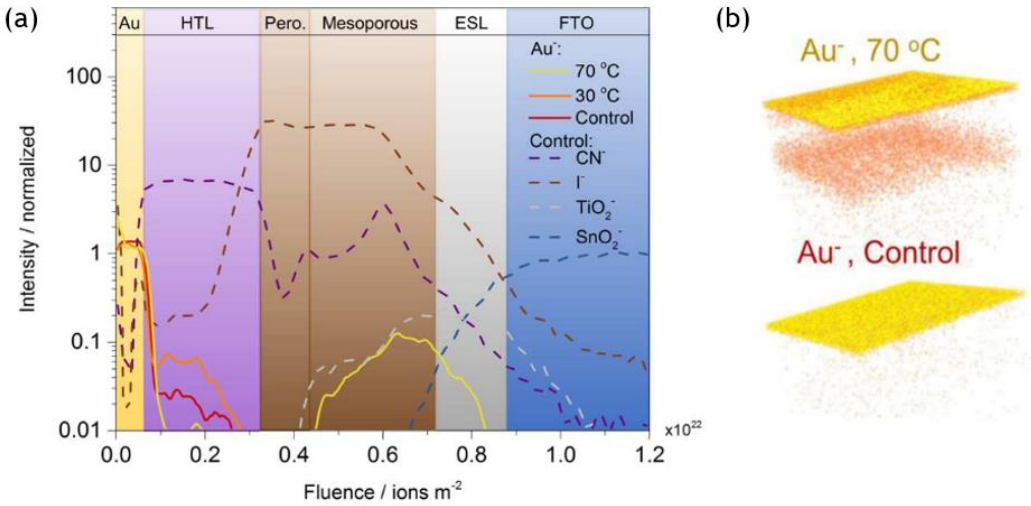

Figure 2.3 - Depth profiles of aged PSC device: (a) profiles of the concentration of selected species across the device, (b) gold migration at 70 °C (adapted from Domanski et al.). [23]

Due to its lower price, appropriate fermi level and high conductivity, silver (Ag) has been proposed to replace Au. However, it still presents stability problems, because Ag films corrode

when in contact with perovskite, forming silver halide, and it often forms shunting paths with the mesoporous TiO_2. [31] Following a different approach, instead of replacing Au, Domanski et al. [23] proposed the insertion of a thin chromium interlayer between HTM and Au, to solve the problem of severe device degradation at elevated temperatures. Their results showed that stability was vastly improved and any degradation was now reversible, demonstrating that the chromium layer hindered the Au diffusion across the HTM. However, this new layer decreases PCE, increases fabrication complexity, and the problems related to the Au (high cost of acquisition and deposition) still remain. [23]

2.2.2 Carbon substitutes

The highlight among all the possible back-contact solutions being investigated are carbon materials, which have already been applied as counter-electrode in DSCs and quantum dot-sensitized solar cells (QDSCs). [32] Their properties, such as abundant sources, low cost, high electrical conductivity, chemical stability, diversity, and suitable work function (5.0 eV, which is near the 5.1 eV from Au fermi level), make them an ideal replacement for the currently used Au. [33] The most known allotropes are diamond, graphite, C60 buckminsterfullerene, graphene and amorphous carbon - Figure 2.4. Each of them have a different bonded patterns of carbon atoms and different dimensions of crystalline structures, which provide them very different chemical and physical properties. The carbon materials found in the literature for this purpose are shown in Table 2.2. [6]

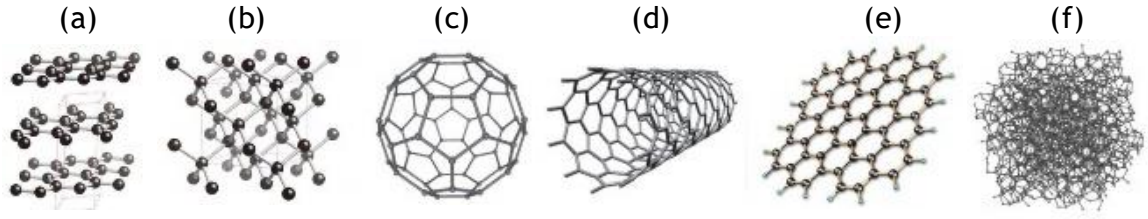

Figure 2.4 - Carbon allotropes: (a) graphite, (b) diamond, (c) C60 buckminsterfullerene, (d) nanotube, (e) graphene and (f) amorphous carbon. [35]

Table 2.2 - Carbon materials used as back contact in PSCs found as far in literature. [6]

Carbon materials	Carbon paste (carbon black with graphite)	Carbon cloth embedded in carbon paste	CNTs	Graphene	3D graphene
Max PCE / %	15.6	15.3	15.2	12.4	10.1

Carbon-based perovskite solar cells (CPSCs) are already well-known in the scientific community. However, the high cell resistance of the thicker stack of the active carbon materials (≈12 –

14 µm) along with the uncontrolled and limited crystallization of the perovskite precursor solution in these thick porous stacks are limiting the significant enhancement of their solar-to-electrical conversion efficiencies. [35]

Nevertheless, there is one carbon allotrope whose low thickness (≈2 nm) allows the above mentioned problems to be overcame: graphene. Its high optical transparency (it transmits 99.7 % of the incident light in the range from infrared to violet) can also open the possibility of lighting the PSC from both sides, increasing cell efficiency and energy production. Furthermore, it also presents high thermal conductivity (≈5x10^3 W·m^{-1}·K^{-1}) at room temperature, large surface to mass ratio (2630 m^2·g^{-1}), superior mechanical properties (i.e., Young's modulus of ≈1 TPa) and high flexibility. [36, 37] Relatively to graphene's unique electrical properties, it is characterized as a semi-metal or zero gap semiconductor and it shows an extraordinarily high electron mobility at room temperature (200 cm^2·V^{-1}·s^{-1}) and low sheet resistance (from 450 Ω·sq). [7, 38, 39]

Another interesting carbon material that is commonly used in fuel cells and electrolyzers applications, but also with potential for solar cells, is carbon paper, which consists of carbon fibers (with ≈7 µm diameter) held together by a carbon matrix. Its manufacturing process is composed by two main heat treatments, carbonization and graphitization, which result in a product with graphite like properties. The features that make it an interesting candidate for perovskite's back-contact are: low electrical resistivity, high flexural/tensile strength, high chemical and mechanical stability, improved thickness uniformity, higher purity, improved durability and low cost. [40, 41] To the best of the authors' knowledge, the use of these materials in solar cells has never been reported in previous studies.

2.3 PSC utilizing carbon papers as back-contact

Carbon paper is a non-woven carbon composite and is the favorite material for the Gas Diffusion Layer (GDL) in PEMFC. Its porosity and gas permeability are carefully controlled because, while the void space provides a free path for diffusion of gaseous species and the removal of the reactant products, the solid part ensures a good electrical and thermal conduction. There is a wide variety of carbon papers, with different treatments, additives and additional layers, in order to adjust its properties to its final application. [41] The influence of the carbon paper's different characteristics in the PSC performance are unknown and further studies are needed to understand its full potential as a PSC back-contact. A certain drawback is its opacity, which decreases its versatility and possible applications.

2.4 PSC utilizing graphene as back-contact

The requirements for a PSC's counter-electrode are: high transparency, high conductivity, chemical stability and charge collecting ability. As we can see from the properties' description above, graphene fulfills by far all the requirements. [6]

Graphene is a two-dimensional (2D), one-atom-thick planar thin layer of sp2-hydridized atoms tightly packed in a hexagonal honeycomb lattice and bonded with each other through covalent bonds, with a molecule bond length of 0.142 nm. Layers of graphene stacked on top of each other form a tree-dimensional (3D) graphite, which has an interplanar spacing of 0.335 nm. It can also be rolled to form one-dimension (1D) carbon nanotubes or wrapped to form zero-dimensional (0D) fullerenes. [36] The first graphene was extracted from graphite in 2004, using a technique called micromechanical cleavage, and since then it has been widely studied and applied within a broad range of applications in the field of electronics, photonics, energy related devices, biomaterials and sensors. [7, 42] In 2010, Andre Geim and Kostya Novoselov were awarded with a Nobel Prize "for groundbreaking experiments regarding the two-dimensional material graphene". [43]

The first attempt to introduce graphene in the PSC composition was made in 2013 by Wang et al, [44] being used as a transparent electrode, between the FTO film and TiO_2 blocking layer. [44] This approach boosted the investigations dedicated to hybrid perovskite solar cells, using graphene as carrier transporting layer (either electron and hole transport materials) and conductive electrode (essentially to replace the conventional TCO). A graphene film can also be used on top of the perovskite as a stability enhancer, due to its weak affinity to moisture and so it prevents the perovskite degradation. [36, 42]

Utilizing graphene as conductive back-contact is relatively new, the first work with this approach having been published only in 2015 by Yan et al. [45] As their PSC did not have a HTM layer, they placed a flexible multilayer graphene (MLG) on top of the perovskite film (with chemically reactive graphene-CH_3NH_3I paste), reaching a PCE of 11.5 %. Apart from a withhold moisture effect, the MLG film enhanced the hole collection and blocked electrons via a Schottky barrier, greatly hindering charge recombination at the interface and demonstrating to be a cheap, stable, high performing, and mechanically robust electrode possibility. [45]

In the same year, You et al. [46] reported a similar approach, but now the PSC had an additional layer of Poly-(3,4-ethylenedioxythiophene): poly(styrenesulfonate) (PEDOT:PSS) between the HTM and graphene layers to decrease the graphene sheet resistance. The resulting PSC was flexible and, due to its transparency level, it can be lighted from both sides, having a PCE of 12.02 % and 11.65 % when lighted from the graphene (double layer) and TCO sides, respectively (PCE of Au control sample was 13.62 %). These results further raise graphene's potential and

versatility as back-contact. [46] The most recent work on this topic was published in 2017 by Wei et al. [47] who used a 3D honeycomb-structured graphene with about 8 layers in a HTM-free PSC, and achieved a PCE of 10.01 %. [47]

2.4.1 Graphene synthesis techniques

Graphene can be synthetized by numerous techniques, including mechanical exfoliation, chemical synthesis, electrochemical exfoliation of graphite, epitaxial growth on silicon carbide, CVD, nanotube unzipping and pyrolysis of sodium ethoxide. [48] Among these techniques, CVD is the most attractive because it allows the synthesis of large area graphene on a wafer scale, with high uniformity and low defects, and enables the exploration of a wide variety of transition metals as catalysts, including nickel (Ni), copper (Cu), ruthenium and cobalt. [49]

In typical CVD, the substrate is placed inside a reaction chamber (commonly a quartz tube inside a horizontal furnace) and heated to a high temperature (900-1100°C) under a flow of an inert gas (usually Argon) and a reduction gas (usually hydrogen). It is then exposed to one or more volatile precursors (gas or liquid that have the pretended film as base atom), which react or decompose on the substrate surface to produce the desired deposit. While the main purpose of the inert gas is to remove impurities from inside the tube and dilute the precursor gas, the reduction gas is used to prevent the metal foil oxidation. Then the samples cool down under a flow of the inert gas. Frequently, volatile sub-products are also produced and are removed by the gas flow. [49, 50]

For graphene CVD-growth, several carbon precursors can be used, such as methane, ethane or benzene. The graphene quality and number of layers (multilayer, few-layer, bilayer, monolayer) are significantly influenced by the properties of the metallic substrate, such as its carbon solubility limit, its crystal structure and lattice parameter, because these determine the growth mechanism of graphene. [49] For instance, single crystal metals are preferred to synthetize monolayer graphene because grains boundaries act as nucleation sites for multilayer growth. [51] Concerning carbon solubility, metals with low carbon solubility (e.g. Cu) are preferred because the growth mechanism, which is surface adsorption during the reaction step, is a self-limiting process and thus easily reproducible and scalable. On the other hand, in metals with high carbon solubility (e.g. Ni) the graphene growth occurs in the cooling step, when the carbon atoms that infiltrated the bulk during the reaction step (high temperature step) come out to the surface and precipitate. In this case, due to the fast cooling process, the growth of monolayer graphene is more difficult to control. Figure 2.5 depicts these two situations. [52]

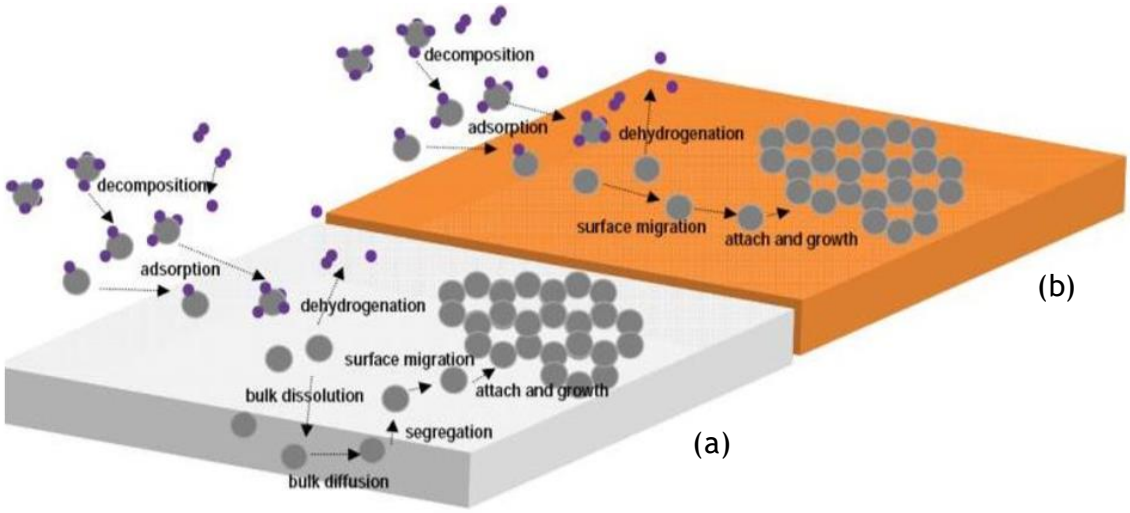

Figure 2.5 - Graphene growth mechanisms on: (a) highly carbon soluble metal substrate and on (b) low carbon soluble metal substrate. [7]

The precursor gas concentration and the thermodynamic parameters, such as temperature and pressure of the system, also have a huge influence on the characteristics of the graphene film obtained. [50] It is verified that monolayer graphene is produced with low precursor concentrations (from 100 ppm to 0.2 % v/v), while the defect density is lower in the graphene samples synthesized at intermediate precursor concentrations (≈0.4 % v/v). At high precursor concentrations (from 2 to 10 % v/v), MLG domains with a monolayer background are formed, indicating that the growth is not self-limiting. However, if working in low pressure conditions, the process becomes self-limiting, allowing the synthesis of graphene with uniform thickness across larger areas, independently of the precursor's concentration. [49] Furthermore, the reaction temperature must be above 800 ºC to allow the pyrolytic cracking of hydrocarbon gases, but must also be under the metal's melting point (1085 ºC for Cu and 1455 ºC for Ni). Due to the high energy consumption, the expensive and precise equipment required, and the possibility of severe physical damage of substrates, other methods are being explored to reduce temperature, such as exchanging the precursor gas for liquid precursors (e.g. benzene) or the CVD conditions (e.g. PCVD). [53]

According to the substrate, the temperature of the reaction step (T_{sub}), gases, and total pressure (P), there are different types of CVD methods, which include Direct Current Discharge CVD (DC-CVD), Radio Frequency – Plasma Enhanced CVD (RF-PECVD), Low Pressure CVD (LP-CVD), Electron Beam Enhanced Plasma CVD (EBEP-CVD), Microwave Plasma Enhanced CVD (MPECVD), Concentric Tube CVD (CTCVD) and Atmospheric Pressure CVD (APCVD). The main characteristics of these CVD variants are presented in Table 2.3. [48]

Table 2.3 - Different types of CVD for graphene synthesis.

Type	Substrate	T_{sub} (°C)	Gases	P (torr)
DC-CVD ($0.5\ A{\cdot}cm^{-2}$)	Si, Ni	950	H_2/CH_4 (92/8)	80
RF-PECVD (400-1200 W)	Ni,Si	600-950	H_2/CH_4	0.02 – 0.4
LP-CVD	Ir(111)	847, 947, 1047	C_2H_4	$7.5x10^{-10}$
CVD	Cu Ni	850, 900 850, 900, 950	CH_4	50
EBEP-CVD	Si (100)	570	H_2/CH_4	0.015 - 0.03
MPECVD	Si	550	H_2/CH_4 (100/5)	1.65
CTCVD	Cu	1010	H_2/CH_4	4
APCVD	Cu	1075	H_2/CH_4	atmospheric

3 Materials and Methods

3.1 Experimental

The experimental work developed within this project is divided in three major parts: PSC device production, carbon paper integration into complete PSC devices, and setup assembly for optimization of graphene synthesis by chemical vapor deposition. All the experiments were performed at UPTEC - Innovation Center laboratory, except the graphene synthesis that was performed at laboratory E101A in the Department of Chemical Engineering.

3.1.1 PSC assembly

Complete PSC devices with gold back-contact were prepared as standard devices, whose production steps will be described next. The selected architecture was mesoporous. Conductive semiconductor PSC glass (from Solaronix) was used as glass substrate for PSC devices - Figure 3.1(a). Several glass pieces with dimensions of 9.6 x 4.8 cm^2 were cut – Figure 3.2(a) - and a laser scribing – Figure 3.2(b) - was made to electrically separate the photoelectrode and the counter-electrode sides. The glass pieces were cleaned accordingly to a standard procedure that includes several steps. First, they were washed with a Hellmanex solution and then with water. After drying with compressed air, the glasses were submerged subsequently in a KOH (Sigma-Aldrich, ≥ 85 %) and ethanol solutions (Valente e Ribeiro. Lda) and subjected to ultra-sounds for 5 minutes - Figure 3.2(c). Next, they were washed with deionized water, dried with compressed air and subjected again to ultra-sounds for 5 more minutes. After drying with compressed air, the TCO side of the substrate was exposed to ultraviolet light for 20 min – Figure 3.2(d).

The first layer being deposited in preparing the complete devices is the blocking layer, made of compact TiO_2 - Figure 3.1(b). For that, a solution of 7 mL of anhydrous isopropanol 99.8 % (Sigma-Aldrich, 99.7%) with 0.4 mL of acetylacetone <<99.5 % (Sigma-Aldrich) and 0.6 mL of titanium diisoropoxide bis(acetylacetonate) 75 %wt (Sigma-Aldrich) was prepared inside a glove box (GB) - Figure 3.2(e). This solution was then brought out of the GB and sprayed - Figure 3.2(h) - uniformly throughout the surface of the substrates placed on a heating plate at 450 ºC - Figure 3.2(i). After 45 min, the set point of the heating plate was changed to 25 ºC. This technique is called spray pyrolysis. The glass pieces were then cut into single cells of 1.2 x 2.4 cm^2 and placed again inside the GB for the deposition of the other active layers.

For the mesoporous layer deposition - Figure 3.1(c), scotch tape was glued onto the counter-electrode side, working as a mask to prevent short circuits in the final device. 1 g of TiO_2 paste (DSL 30NR-D from DyeSol) was dissolved in 6 g of ethanol; 50 μL of this solution were spin-

coated on each device - Figure 3.2(f). After the deposition, the cells were placed on a heating plate at 100 °C for 1 min and then sintered at 500 °C for 2 h in an oven – Figure 3.2(g).

After allowing the mesoporous layer to cool down to room temperature, follows the perovskite deposition inside the GB. The components chosen for the perovskite's monovalent cations were a mixture of FA, MA and inorganic Cs, because the resulting triple cation perovskite composition is thermally more stable, contains less phase impurities and is less sensitive to processing conditions. [54] For the inorganic cation and halogen, lead and a mixture of iodine and bromine were used, respectively. Thus, the perovskite solution is prepared as follows: 0.50711 g of PbI_2 (1.1 M) (ACROS ORGANICS, 99 %), 0.073402 g of $PbBr_2$ (0.2 M) (Sigma-Aldrich, ≤ 98 %), 0.022394 g of MABr (0.2 M) (Dyesol) and 0.17197 g of FAI (1 M) (Sigma-Aldrich) were first weighed and mixed. Then 0.8 mL of DMF (dimethylformamide) (Sigma-Aldrich, 99.8%) and 0.2 mL of DMSO (dimethyl sulfoxide) (Sigma-Aldrich) were added. Finally, 0.95 mL of this stock solution were added to 0.05 mL of a cesium iodide solution (Sigma-Aldrich); 50 µL of this solution were spin-coated on top of the TiO_2 mesoporous layer. The method selected for the perovskite deposition was the one-step deposition via anti-solvent and thereby 100 µL of chlorobenzene (Sigma-Aldrich, 99.8 %) were dripped onto the cell during the spinning. Its function was to delay the perovskite crystallization and enable the formation of a dense and more uniform surface. [18] The cells were then placed on a heating plate at 100 °C for 40 min, and left to cool down to room temperature.

Next was the deposition of the HTM layer, which was spiroOMeTAD - Figure 3.1(e). First, 0.102 g of this compound (Chemborun, 99.57 %) was weighted and dissolved in a solution made of 1116 µL of chlorobenzene, 40 µL of 4-tert-butylpyridine (TBP) (Sigma-Aldrich), 23 µL of lithium bis(trifluoromethanesulfonyl)imide (LiTFSi) (ACROS ORGANICS) and 10 µL of cobalt (III) TFSI salt from Dyesol (FK209). Then, 50 µL of this stock solution were spin-coated on each cell, inside the GB, and left to dry at ambient temperature. The last step of the PSC assembly was the gold deposition - Figure 3.1(f) - by a thermal evaporation process - Figure 3.1(j).

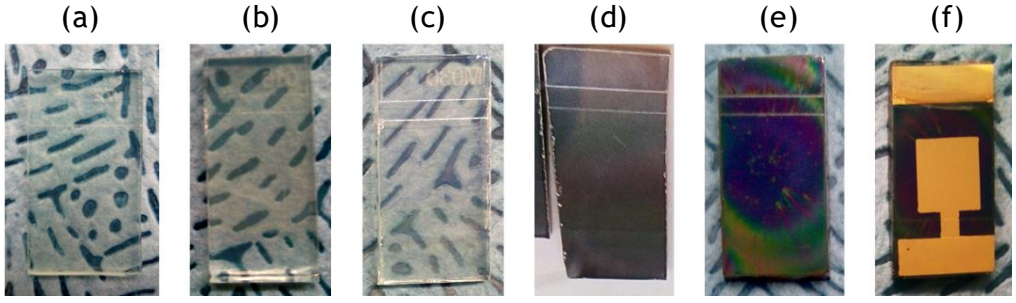

Figure 3.1 – PSC layers deposition: (a) glass substrate, (b) compact TiO_2, (c) mesoporous TiO_2, (d) Perovskite, (e) spiroOMeTAD and (f) gold back-contact.

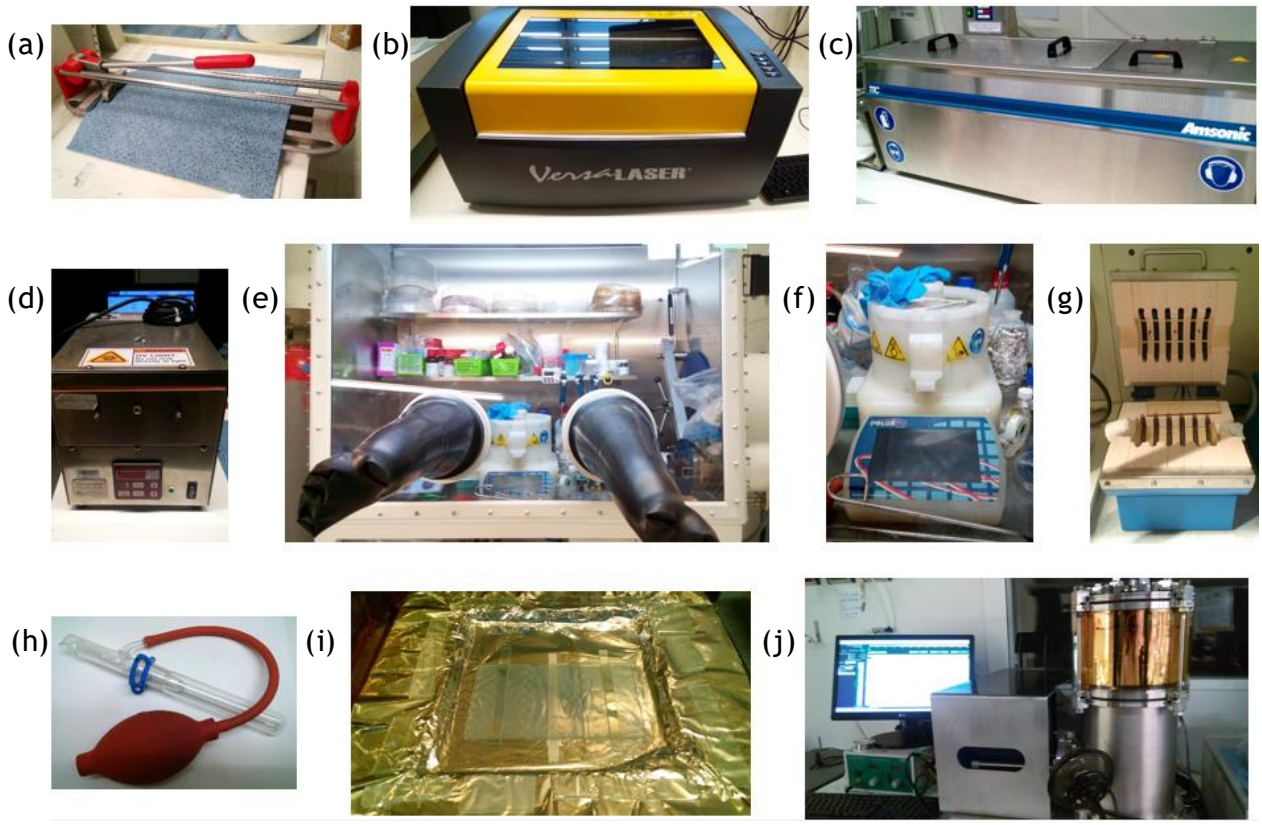

Figure 3.2 – Equipment required for the PSC fabrication: (a) glass cutter, (b) laser system (VersaLaser), (c) ultrasonic cleaning (Amsonic), (d) UV-rays system (Jelight), (e) glove box, (f) spincoater (SPS-Europe, POLOS), (g) oven (Thermolab), (h) spray instrument, (i) spray pyrolysis setup and (j) thermal evaporator (Oxford vacuum science).

3.1.2 Carbon paper preparation and assembly on the PSC

Each PSC was first tested with Au as back-contact and then the Au was peeled off with scotch tape - Figure 3.4(a) - and two different carbon papers were tested with four different adhesion layers. So, for attaching the carbon papers to the PSC device an adhesion layer was needed to promote good contact between the carbon paper and the HTM layer. This adhesion layer must present high conductivity and a work function between the HTM and the carbon material. So, it was selected typical hole transport materials as spiroOMeTAD and PEDOT:PSS (Sigma-Aldrich, 3.0-4.0% in H_2O). 20 µl of the adhesion layer were dropped onto the 1 x 1 cm^2 pieces of carbon paper, then carefully spread and partially dried with a nitrogen gun - impregnation technique. The tested carbon papers were 28BC and 39AA (SIGRACET) - Figure 3.3.

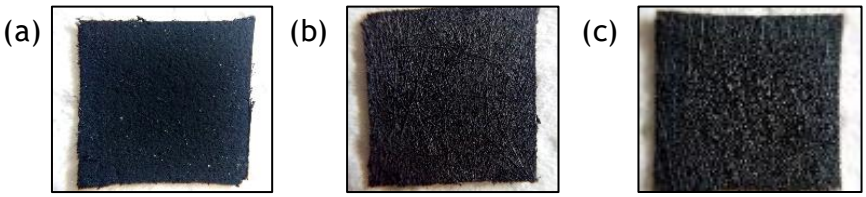

Figure 3.3 - Carbon papers: (a) 28BC front side, (b) 28BC back side and (c) 39AA.

PEDOT:PSS was tested pure and with two different additives, studied separately: *D*-sorbitol (150 mg·mL^{-1}) (Sigma-Aldrich ≥ 98 %) and isopropanol (1:1 ratio). The PEDOT:PSS solution with isopropanol was the only one spincoated onto the carbon papers at 2500 rpm during 30 s. Carbon papers tested with spiroOMeTAD were dried at 60 °C during 15 min before being incorporated into the final device, while the ones with PEDOT:PSS were dried at 120 °C during 90 min, to ensure total evaporation of its dispersing agent (water). Then, the papers were placed on the PSC device - Figure 3.4(b), followed by copper tape (3M) (just to make the metallic contact with the external circuit), a thin film of Polydimethylsiloxane (PDMS) - Figure 3.4(c) - and a glass piece - Figure 3.4(d). Finally the structure was fastened mechanically - Figure 3.4(e). A PDMS layer was made by mixing 3 g of silicone elastomer (SYLGARD 184) with 0.3 g of silicone elastomer curing agent (SYLGARD 184), which was then cured at 60 °C during 30 min and cut with a scalpel down to the appropriate size.

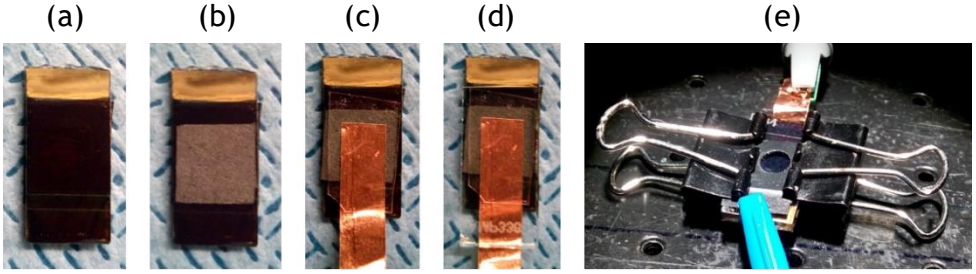

Figure 3.4 - PSC assembling: (a) PSC without back-contact, PSC with (b) the carbon paper, (c) copper tape, PDMS film and (d) glass piece. (e) The final assembled device connected to the external circuit.

3.1.3 Graphene synthesis by Chemical Vapor Deposition

Copper substrates were deposited by magnetron sputtering (MANTIS, UK) - Figure 3.6(c) - onto silicon dioxide on silicon (SiO_2/Si) wafers with a diameter of 5 cm - Figure 3.5 - and cut into smaller samples of about 1 cm^2. Then, two samples were carefully introduced inside the quartz tube with an inner diameter of 7.5 cm and a length of 152 cm (supported by a quartz piece), and oxygen and other impurities were removed from the tube by varying the Argon (Ar) flow during a cleaning time, to create turbulence and clean the stagnant gases.

Figure 3.5 - SiO_2/Si wafer coated with Cu by sputtering.

The furnace - Figure 3.6(a) - was then heated to a temperature of 1000 °C at a slow rate of 3 °C·min^{-1} and under an argon (inert gas) flow of 200 mL·min^{-1} - Figure 3.6(b). During this heating step, impurities were removed from the chamber and the metal foil was annealed. When the set temperature was reached, the Ar flow was stopped, methane (CH_4) and hydrogen (H_2) started flowing and the temperature was kept constant. After a defined reaction time, the CH_4

and H_2 flows were stopped and the Ar flow restarted at a decreased rate of 150 mL·min^{-1} while the furnace cooled down to room temperature, also at a 3ºC/min rate. The sample was finally removed from the tube and carefully stored for characterization.

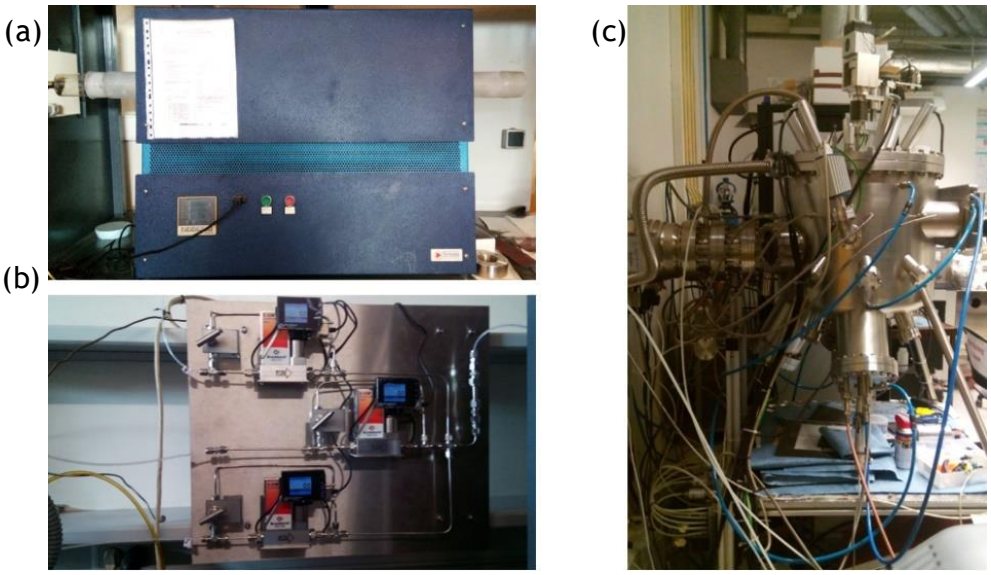

Figure 3.6 - CVD installation: (a) Horizontal oven with a quartz tube, (b) flowmeters setup and connection tubes and (c) magnetron sputtering system.

3.2 Characterization techniques

3.2.1 Raman spectroscopy

A Raman spectrometer (LabRAM - Jobin Yvon) was used to identify the compounds formed in the CVD process, through the comparison to Raman spectra found in literature. In the case of graphene, its Raman spectrum can reveal the number of graphene layers and the quantity of defects by the analysis of three characteristic peaks, denominated as D, G and 2D, which are located around 1350 cm^{-1}, 1587 cm^{-1} and 2658 cm^{-1}, respectively. [55]

3.2.2 X-Ray diffraction (XRD)

XRD diffractograms were obtained with an X-Ray diffractometer (Rigaku SmartLab) to assess the CVD products through comparison with XRD diffractograms found in literature.

3.2.3 Scanning electron microscopy (SEM) analysis

Morphology and thickness of the copper deposited by magnetron sputtering was analyzed using a scanning electron microscope (Phenom XL).

3.2.4 Atomic force microscopy (AFM)

Atomic force microscopy was used to characterize the surface roughness and determine the thickness of the copper deposited by magnetron sputtering.

3.2.5 Scanning Kelvin probe microscopy (SKPM)

To determine the work function of the carbon papers ($WF_{material}$), an ultra-high vacuum Kelvin Probe (KPTechnology, Series 10) was used, at ambient pressure, to determine the contact potential difference (*CPD*) of each sample, which allowed for the calculation of the respective work function with equation (1), where the WF_{tip} is ≈4.65 eV. [56]

$$WF_{material} = WF_{tip} + CPD \quad (1)$$

3.2.6 Solar cell performance evaluation

The solar cell performance was evaluated using a photocurrent-voltage (*I-V*) characteristic curve, which was measured by a ZENNIUM workstation (Zahner Elektrik, Germany) controlled by Thales software package (Thales Z 2.0). The measurements were performed at 25 °C, under a set point simulated sunlight intensity of 1 sun (100 $mW \cdot cm^{-2}$), calibrated with a c-Si photodiode. A characteristic curve was obtained for each cell by applying an external potential bias (*V*) to the cell, from negative values to positive, and measuring the generated current (*I*). The measured *I* values were then corrected for the sample area that was effectively illuminated by the simulator. Through the *I-V* characteristic curve, it was possible to calculate the open-circuit voltage V_{OC} (voltage value when no current is flowing), short-circuit current I_{SC} (current value when voltage is zero), current and voltage at maximum power point (I_{MMP}, V_{MMP} and P_{MMP}) respectively), *FF* (ratio between the maximum power value and the maximum theoretical power value) – equation (2) - and the efficiency (η) of each cell (ratio between the power generated and the power of the incident light I_S) – equation (3).

$$FF = \frac{I_{MMP} \times V_{MMP}}{V_{oc} \times I_{sc}} \quad (2)$$

$$\eta = \frac{FF \times V_{oc} \times I_{sc}}{I_s} \quad (3)$$

4 Results and discussion

4.1 Carbon paper experiments

Carbon materials have been widely studied for use as back-contact in PSCs. Nevertheless, so far no document was found in literature using carbon papers specifically. Two different carbon papers were used, from what was currently available at the lab: 28BC and 39AA from Sigracet®. These carbon papers were specifically designed for GDLs in PEMFC, and so their structure and characteristics are optimized for this purpose and not for solar cells - Figure 4.1. However, their good conductivity, adequate work function and versatility in the integration into final devices make it possible for these to be applied as back-contact in PSCs. Moreover, for large-scale applications, having a material with such an easy deposition step is a huge advantage. On the other hand, the porosity of the carbon paper also increases the back-contact active surface area, since charge recombination, instead of occurring on a 2D plane, will occur in the porous 3D structure, thus improving the overall power conversion efficiency.

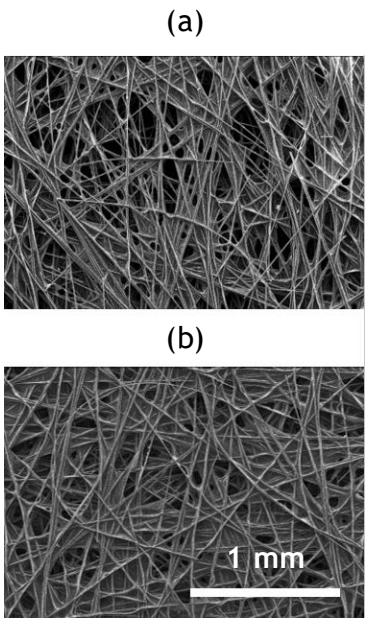

Figure 4.1 - *SEM images of carbon paper with different filler content: GDL backing with (a) high porosity and (b) low porosity.*

Two different adhesion layers were impregnated into the carbon paper to fill its pores and create a capping layer enhancing the contact between the carbon paper and the PSC's HTM - Figure 4.2.

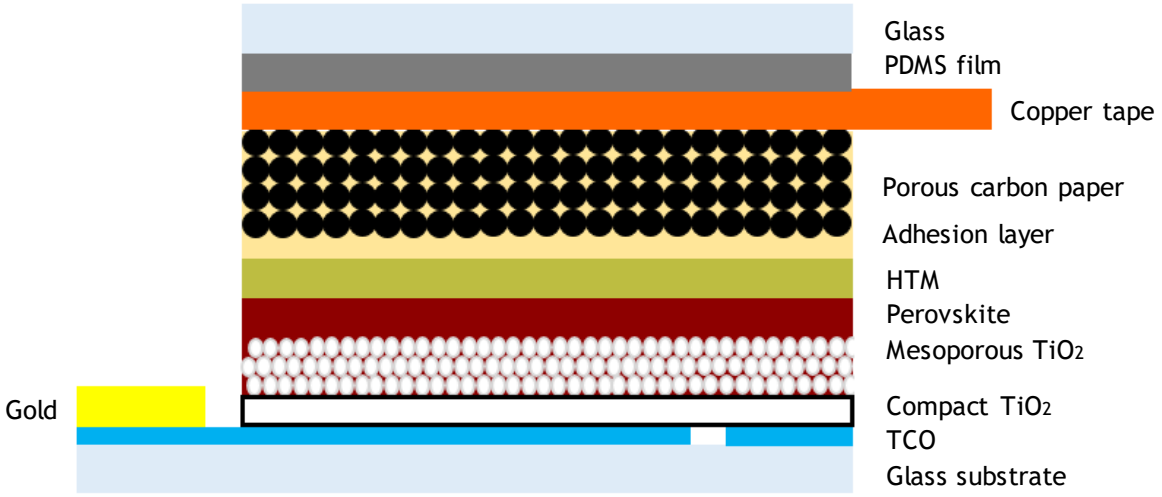

Figure 4.2 – Illustrative scheme of a PSC device with carbon paper as back-contact.

The main features of a good adhesion layer are high conductivity, good ability for transporting holes and blocking electrons, good energy levels alignment (between the -5.2 eV from the spiroOMeTAD HOMO level and the ≈-4.7 eV work function of the carbon paper) and high chemical affinity with the interfaces. Table 4.1 presents the properties of the two selected adhesion layers: spiroOMeTAD and PEDOT:PSS. SpiroOMeTAD is the HTM used in the best-performing PSC devices and is the HTM used in the PSC cells of this study, therefore significant energy losses due to different fermi levels alignment will not occur, and neither will problems due to degradation caused by undesirable reactions at the interface. PEDOT:PSS was selected not only due to its high conductivity and suitable work function, but also because remarkable results have been presented by Pen You et al. [46] by using this material as adhesion layer between graphene and spiroOMeTAD HTM in a PSC device. [46]

Table 4.1 - Conductivity, carrier mobility and work function values for the two adhesion layers studied.

Adhesion layer	Conductivity / $S \cdot cm^{-1}$	Carrier mobility / $cm^2 \cdot V^{-1}s^{-1}$	Work function / eV
spiroOMeTAD	2×10^{-5} [57]	3×10^{-4} [58]	-5.2 [57]
PEDOT:PSS	4×10^{-4} [59]	9.5×10^{-3} [60]	-5.1 [59]

Standard devices with gold back-contact were prepared as described in Chapter 3. Then each PSC was tested nine times: the first time with gold, which was later peeled off for the carbon papers characterization, and then eight times for the different carbon papers (two carbon papers with four different adhesion layers). Thereby, in the same batch of cells, each cell is characterized for the eight different back-contact configurations, ensuring differences are only due to properties of the carbon paper/adhesion layer system and not due to low reproducibility in the deposition of the adhesion layers. This is only possible because the carbon papers do not irreversibly adhere to the PSC and the deposited adhesion layer does not degrade with time and usage. Therefore, non-uniformities or different thicknesses of the adhesion layers will not influence the results' variability in the different cells of the same batch. The only exception was for the carbon paper 28BC with *D*-sorbitol solution, which was shown to be glued onto the PSC surface. Thus, this configuration was always the last one to be characterized and each cell had a different carbon paper substrate.

Since the area-specific resistance through-plane (ASR_{TP}) of the carbon papers decreases with pressure (until a certain value after which the carbon fibers collapse), the two clamps that fasten the two glass substrates were chosen carefully according to their strength. Additionally, a thin and flexible PDMS layer was added between the paper and the glass to prevent the collapse of the carbon papers fibers. [61] The ability of the carbon papers to maintain their properties throughout the measurements, even when subjected to relatively high pressures, is

favorable to their commercial application since it is an indication of high chemical and mechanical stability.

4.1.1 Adhesion layer effect

Regarding the study of different adhesion layers, experiments were first done without any adhesion layer by just applying pressure between the two contacts; very low efficiencies (below 0.04 % - results not shown) were obtained, which corroborates the importance of having a very good interface contact between the HTM and the back-contact, and consequently the need to use an engineered adhesion layer.

PEDOT:PSS as adhesion layer was firstly deposited by the impregnation technique, which did not ensure a high uniformity after deposition and consequently resulted in low reproducibility. As an attempt to increase the deposition uniformity, this adhesion layer was spincoated on top of the carbon paper. However, PEDOT:PSS is dispersed in water and, as the carbon paper is hydrophobic, the PEDOT:PSS dispersion is thrown out during the spin. To decrease the surface tension and thus allow the use of spin coating and facilitate PEDOT:PSS penetration into the pores, isopropanol was added to PEDOT:PSS in a ratio of 1:1 - Figure 4.3.

(a) 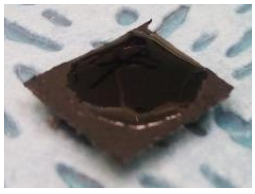 (b) 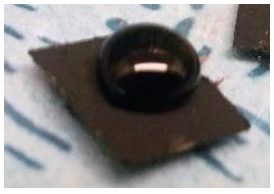

Figure 4.3 - PEDOT:PSS (a) with and (b) without isopropanol on a 28BC carbon paper.

Still concerning PEDOT:PSS deposition optimization, it has been reported that adding a processing additive such as *D*-sorbitol resulted in further reorganization and stabilization of the PEDOT and PSS chains by a plasticizing effect during subsequent thermal annealing of the films. This is responsible for an enhanced environmental stability, improved interface contact and increased conductivity of the PEDOT:PSS thin films. [59] Therefore, a new solution of PEDOT:PSS was made with *D*-sorbitol, with a concentration of 150 $mg \cdot mL^{-1}$, according to the optimum value reported by Peng You et al. [46] Finally, PEDOT:PSS is extremely hygroscopic and PSCs are quickly degraded when in contact with water. Hence, the carbon papers with PEDOT:PSS were stored inside the glove box immediately after curing , to prevent water absorption.

Since spiroOMeTAD is hydrophobic, it penetrates into the pores and adheres to carbon fibers very easily and so a uniform capping layer is formed. Therefore, the impregnation technique allowed an efficient pore filling with reproducible deposition.

Table 4.2 presents the photovoltaic performance parameters (η, V_{oc}, I_{sc} and *FF*) of different carbon paper/adhesion layer configurations. Table 4.3 shows the ratio between the photovoltaic performance parameters of these configurations and the respective cell with the reference back-contact (gold). A batch of standard perovskite solar cells composed by 8 cells usually present a reproducibility no higher than 80 %. Thus, a performance analysis relative to the reference PSCs allows for the elimination of the inner experimental variants that are related to the PSC's conventional production process and the perception of the real effect of substituting the gold back-contact by other materials. Box charts with the average, maximum and minimum values for each parameter, for the obtained and ratio values (comparatively to the reference), are presented in Appendix 2, reflecting exactly these deviations.

The obtained performance ratios for the different PEDOT:PSS solutions used were very similar. However, PEDOT:PSS's bare solution presented a slightly better photovoltaic performance for both carbon papers. Isopropanol was added to reduce its surface tension and thus the pore filling and surface uniformity was improved and a slightly more reproducible deposition process was obtained. Nevertheless, by adding isopropanol the PEDOT:PSS concentration in water decreases by half, which compromises its properties, such as conductivity and carrier mobility. Moreover, even if the spin coating process is able to improve the reproducibility of the deposition, it can also cause a deficient pore filling of the porous carbon paper as well as a poor contact interface between the carbon paper/PEDOT:PSS adhesion layer due to the adhesion layer being thrown out during the spin.

In what concerns the *D*-sorbitol additive, it was empirically verified that it increased the PEDOT:PSS adhesion to the PSC, however, the conductivity and stability enhancement described above are only obtained after an optimized thermal annealing process. In this study the annealing procedure used for the PEDOT:PSS with *D*-sorbitol additive was the same used for the other PEDOT:PSS solutions, which was probably not the most suited to optimizing the plasticizing effect. The optimization of the thermal annealing step as well as the concentration should be further investigated.

SpiroOMeTAD results are much lower than PEDOT:PSS results. Its conductivity and carrier mobility, despite being lower than the values from PEDOT:PSS, should not be the main reason for the different values between both HTM, because the higher resistance to the electron flow is located at the interfaces. Then, it is assigned that SpiroOMeTAD has less affinity with the carbon paper than PEDOT:PSS. The reason behind this difference needs further investigation.

Table 4.2 - Maximum and average (between parentheses) values of η, V_{oc}, I_{sc} and FF of the PSC with carbon papers as back-contact.

Back-contact	Adhesion Layer	η / % (average)	V_{oc} / V (average)	I_{sc} / mA·cm^{-2} (average)	*FF* (average)
Au	-	15.05 (12.05)	1.03 (0.97)	21.79 (17.65)	0.7 (0.63)
Carbon paper 28BC	PEDOT:PSS	6.91 (5.05)	1.02 (0.96)	10.34 (8.72)	0.60 (0.54)
	PEDOT:PSS + *D*-sorbitol	5.55 (4.63)	1.00 (0.94)	10.70 (9.10)	0.59 (0.53)
	PEDOT:PSS + Isopropanol	6.25 (4.58)	1.02 (0.97)	10.62 (8.23)	0.58 (0.53)
	spiroOMeTAD	3.30 (2.13)	1.01 (0.95)	5.93 (4.12)	0.58 (0.53)
Carbon paper 39AA	PEDOT:PSS	1.68 (0.79)	0.98 (0.61)	4.21 (2.67)	0.47 (0.35)
	PEDOT:PSS + *D*-sorbitol	1.18 (0.59)	0.76 (0.56)	3.07 (1.93)	0.55 (0.41)
	PEDOT:PSS + Isopropanol	1.35 (0.59)	0.94 (0.67)	3.23 (2.18)	0.44 (0.35)
	spiroOMeTAD	0.62 (0.40)	0.98 (0.59)	3.33 (1.53)	0.43 (0.34)

Table 4.3 - Maximum and average (between parentheses) values of the ratio between the η, V_{oc}, I_{sc} and FF obtained with the PSCs with carbon papers and gold as back-contact.

Carbon paper	Adhesion Layer	η_{CP}/η_{Au} / % (average)	$V_{oc\,CP}/V_{oc\,Au}$ / % (average)	$I_{sc\,CP}/I_{sc\,Au}$ / % (average)	FF_{CP}/FF_{Au} / % (average)
28BC	PEDOT:PSS	55 (38)	104 (100)	72 (45)	99 (85)
	PEDOT:PSS + *D*-sorbitol	49 (38)	103 (98)	53 (47)	99 (82)
	PEDOT:PSS + Isopropanol	52 (35)	104 (101)	69 (44)	98 (83)
	spiroOMeTAD	26 (16)	102 (99)	42 (22)	99 (83)
39AA	PEDOT:PSS	13 (6)	106 (63)	38 (16)	79 (56)
	PEDOT:PSS + *D*-sorbitol	11 (4)	79 (58)	16 (10)	86 (63)
	PEDOT:PSS + Isopropanol	12 (5)	95 (70)	18 (12)	75 (56)
	spiroOMeTAD	11 (3)	99 (62)	19 (9)	80 (54)

4.1.2 Carbon papers effect

Both papers analyzed from Sigracet® present a code name, being the first digit related to thickness and the second digit related to porosity - Table 4.4. The AA refers to a fully graphitized carbon fiber substrate, while the BC refers to a hydrophobized substrate (5 wt.% PTFE) coated with a microporous layer (MPL) based on 77 wt.% carbon black and 23 wt.% PTFE (optimum levels of porosity and hydrophobicity for PEMFC), which improves durability and stack performance. [61] Despite the better results, the BC carbon paper family is not as conductive as the AA carbon fiber substrates – Table 4.4. This conductivity difference, even if not very significant, can be explained by the different treatments the papers are subjected to. AA carbon papers are fully graphitized, i.e. the carbonizable resins that were impregnated into the raw carbon fiber paper during its manufacture are turned into graphite by curing whose purpose is to adjust the porosity and to enhance electrical and thermal conductivity. [62] BC papers are also subjected to graphitization, but afterwards a hydrophobic treatment with PTFE is applied to increase hydrophobicity, gas permeability and to decrease the porosity. Then, a MPL is added to decrease carbon paper porosity and permeability but increasing the electrical resistivity. [61, 63]

Table 4.4 – Thickness, porosity, pore diameter and conductivity of 28BC and 39AA carbon papers.

Carbon Paper	Thickness / µm	Porosity / %	Pore Diameter / µm	Conductivity / $S \cdot cm^{-1}$
28BC	235	36 – 37	0.1 - 0.3 *	2.4 – 2.7 **
39AA	280	89	42 – 44	4 – 5 **

*Only for the MPL

**Under 1 MPa pressure

In small cells like the ones used in this study (< 1 cm^2), the most significant electrical resistivity associated to the back-contact is determined within the back-contact/adhesion layer/HTM interfaces, and not the electrical resistivity of the back-contact material itself. Thus, the most important factors that come into play in the interfacial contact resistivities are the contact surface areas, energy levels alignment allowing charges to flow with minimal losses, and chemical affinity of the materials. Since it is at the interface between the back-contact material and the adhesion layer that the electrons that come from the external circuit recombine with holes from the HTM, a good interface contact will allow a greater rate of charge carrier's recombination, resulting in improved photovoltaic performance. Analyzing again Table 4.4 for an overview of the different carbon paper/adhesion layer configurations, it can be concluded that 28BC carbon paper allows for better photovoltaic performance parameters (η, V_{oc}, I_{sc} and *FF*). Looking at the main structural differences between the two papers, there are two main differences that might justify these photovoltaic performance differences: porosity and pore diameter. A larger surface area is reached by the material with higher porosity and

smaller pore diameter. The 39AA is ≈2.5 times more porous than the 28BC, however the pore diameter difference between the papers is much larger: the pore diameter of the MPL of the 28BC is ≈215 times smaller than the diameter of the 39AA pores - Table 4.4. Thus, it is expected that the 28BC has a larger contact interfacial area, which will influence the interfacial contact resistivity and consequently the collection of charges in the back-contact.

This conclusion might be further validated by a closer look at the photovoltaic performance parameters. The *I-V* and power curves of the PSC with the best efficiency for each papers (carbon papers with PEDOT:PSS bare solution) are presented in Figure 4.4.

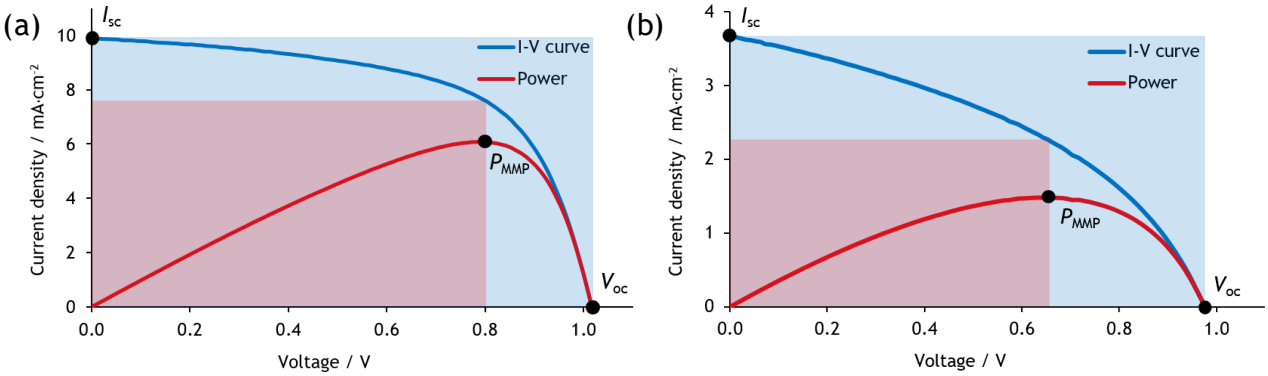

Figure 4.4 - I-V and power curves of the PSC with the best efficiency for (a) 28BC and (b) 39AA carbon papers (carbon papers with PEDOT:PSS bare solution), with the V_{oc}, I_{sc}, P_{MMP} and the rectangles that allow the calculation of the FF.

When a load is present in a solar cell, a potential difference is developed between the two electrodes of the cell. This potential difference generates a forward current which flows in the opposite direction of the photocurrent (reverse current). The highest electrical potential difference obtained for a solar cell is under open-circuit conditions (V_{oc}) when there is no current flowing through it. In an illuminated open circuit PSC, the photo-induced electrons and holes pairs in the perovskite will be pulled into the corresponding p-type (perovskite/spiroOMeTAD interface) and n-type (perovskite/TiO_2 interface) regions, i.e. holes move to the HTM while electrons move to the TiO_2 mesoporous layer, creating a potential difference across the solar cell. This created forward bias current is in the opposite direction to the light generated current (reverse bias) and both currents are flowing simultaneously. The V_{oc} occurs when the forward bias current exactly balances the light generated current, i.e. the net current null. [64]

The factors that most influence the V_{oc} are: reverse saturation current, temperature and illumination intensity, carrier density, defect states and crystallinity, morphology, recombination, donor–acceptor interface area and electrodes work function. [65] Since within this study the back-contact is the only element modified, the last two factors are the predominant ones. As the papers are graphitic, their work function should be close to ≈-4.6 eV.

In fact, the work function values measured by SKMP technique for carbon papers 28BC and 39AA are -4.74 eV and -4.81 eV, respectively, which is aligned with the energy levels of the overall structure. Nevertheless, an improved interface contact is observed for the 28BC carbon paper, which may be responsible for an improved interfacial charge recombination pathway, and thus higher open-circuit voltages.

The fill factor (*FF*) parameter is a measurement of the quality of a solar cell, because the higher its value, the closer the cell's output power is to its theoretical. It is given by equation 2 and in Figure 4.4 it is the ratio between the red and the blue rectangles. A high *FF* is obtained for devices with high shunt resistances and low series resistances. The shunt resistance accounts for the existence of alternate current pathways through a photovoltaic cell, and it should be as high as possible to prevent current leakage through these alternate paths. The series resistance accounts for energetic barriers at interfaces and bulk resistances within layers. It can be decreased by ensuring a proper energy level alignment of the different layers, by decreasing the interface resistances or by decreasing the charge carrier recombination rate. [66] Assuming a proper band alignment, interface resistances are the key causes of the low *FF* values of the 39AA carbon paper. Actually as noticed in Figure 4.4, a pronounced decrease in the shunt resistance and an increase in series resistance occurred for the 39 AA carbon paper. The carbon paper 28BC also presents some series resistance and a low shunt resistance when compared to reference PSC device, meaning that the interface contact in the counter-electrode of the cell can be improved. It should also be pointed out that there is an additional interface (between the adhesion layer/HTM) that will create a new interfacial resistance which could increase the series resistance, contributing for a lower *FF* value.

Short-circuit current (I_{sc}) is the current flowing in the cell caused by light-generated carriers that still flow through the solar cell when there is no potential difference. As the I_{sc} and the light-generated current are identical, this short-circuit current is the largest current which may be drawn from the solar cell. [67] Its value depends essentially on four processes: photon harvesting, photoelectron injection, perovskite regeneration and electron extraction. The first process depends on the power and spectrum of the incident light, on the PSC illuminated area and on optical properties as absorption and reflection; all these variables are kept constant in all experiments. [68] Photoelectron injection and perovskite regeneration are independent of the back-contact and so they are taken into account within this study. Finally, electron extraction rate is directly related to back-contact/HTM interfacial contact, being higher for lower interfacial resistivities. Since a higher I_{sc} is reached for a higher net electron extraction rate, this corroborates the carbon papers photovoltaic performance presented above. It is also worth mentioning that the I_{sc} and V_{oc} value can be enhanced if the work functions of the carbon papers are closer to (but still higher than) the HTM work function (≈-5.1 eV), to minimize energy

loss during the electron flow in the different layers. Although, the 28BC work function is just 70 meV closer to -5.1 eV than the 39AA work function, which is not significant.

Among the photovoltaic performance ratios for all adhesion layers studied for the 28BC carbon paper, I_{sc} is the one whose values are furthest from 100 %. I_{sc} is mainly limited by the low electron extraction rate; this reduced extraction rate can occur in four regions of the PSC: adhesion layer-HTM interface, adhesion layer bulk, adhesion layer-carbon paper interface, and carbon paper bulk. Table 4.5 shows possible courses of action to decrease the resistance in each of these zones.

Table 4.5 - Possible actions to increase the electron extraction rate, with the correspondent consequence and intervention zone.

Action	Consequence	Adhesion layer-HTM interface	Adhesion layer bulk	Adhesion layer-carbon paper interface	Carbon paper bulk
Use a smoother carbon paper	Greater surface contact area between the two layers	✓			
Use a more conductive carbon paper	Optimization of the carbon paper conductivity				✓
Use a carbon paper with a work function slightly above -5.1 eV	Reduction of interfacial energy losses due to the approximation of the different fermi levels			✓	
Adjust the pressure of the fasten method	Optimization of the carbon paper conductivity				✓
Use a carbon paper with smaller pore diameter	Higher adhesion layer/carbon paper potential contact interfacial area			✓	
Improve the impregnation process	Lower interfacial resistance			✓	
Adjusting the additive *D*-sorbitol concentration	Better PEDOT:PSS overall properties	✓	✓	✓	
Optimizing the cure overall process	Better adhesion layer overall properties	✓	✓	✓	
Acquire an hydrophilic carbon paper	Total pore filling due to the facilitation of the PEDOT:PSS penetration without adding surfactants			✓	
Produce (by polymerization) PEDOT:PSS within the carbon paper pores	Improve the overall properties of PEDOT:PSS	✓	✓	✓	

Carbon papers have never been reported for solar cell applications, emphasizing the novelty of the present work. Moreover, very promising power conversion efficiencies were obtained, giving room to increase the overall efficiency by optimizing and adjusting several experimental procedures, which were detailed, explored and explained in this section.

4.2 CVD Experiments

Before starting performing CVD experiments, a detailed review of the state of art concerning graphene growth by chemical vapor deposition was performed to assess the most relevant operating parameters, the best experimental procedures, and to define an experimental design applicable to the available experimental setup – Figure 3.6.

The following operating conditions should be considered for a CVD: heating and cooling rates, pressure, carbon precursor type and concentration, reducing agent (hydrogen), metallic substrate, reaction time and temperature, concentration ratio of hydrogen and carbon precursor during CVD reaction. The relevance of these parameters will be discussed next.

It is important to mention that the goal of the present task is to give the first steps in the development of a transparent back-contact for perovskite solar cells, and graphene can be used for this purpose. However, for this application, one of the most important properties needed in the produced graphene is high conductivity. It is reported that graphene's conductivity increases with the number of layers - Figure 4.5 - but, if so, transparency may be compromised. Attempting a balance of conductivity vs. transparency for multilayers, it is known that the transparency decrease is not as significant when compared to the conductivity enhancement: the transparency of few-layer graphene (FLG, 2-3 layers) and multilayer graphene (MLG, 12-14 layers) is, respectively, 96.4 % and 89.6 % (i.e. decrease of 7 %), while the resistivity is ≈360 Ω·cm and ≈142 Ω·cm (i.e. decrease of 60 %), respectively. As the work function of graphene is almost independent from the number of layers (≈-4.55 eV for monolayer and ≈-4.6 eV for graphite), the following optimization process was envisaged to produce MLG. [69-72]

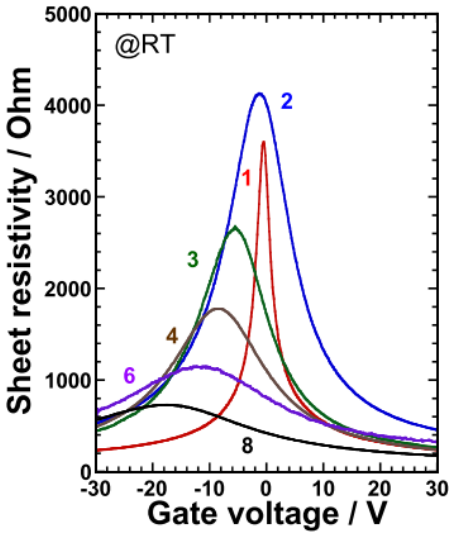

Figure 4.5 - Sheet resistivity of graphene with different number of layer as function of gate voltage.

4.2.1 Operating Conditions

As it is possible to produce high quality graphene under ambient pressure, no vacuum system was considered to minimize costs and to guaranty the possibility of scalability. [73] The heating and cooling rates used were 3 $^{\circ}C \cdot min^{-1}$; it is important to mention that no cooling system (e.g. chiller) is coupled to the oven to allow for a faster cooling rate. Another factor that was not controllable was the quartz tube size: 7.5 cm diameter and 152 cm length. However, the dimensions of the quartz tube will not influence the final results, because an appropriate atmosphere for graphene growth is still created. The only drawback of using a big tube is that a higher amount of gas reagents was spent.

Nickel and copper are the most common CVD metallic substrates. In this process, the metallic substrate also acts as the catalyst, since it enables the reaction to occur at its surface. [74] As Ni has a high carbon solubility (1.15 % for a 700 nm Ni film at 1000 °C), the carbon atoms diffuse into the nickel bulk during the high temperature period and, during the cooling step, the saturated carbon atoms segregate back to the surface and precipitate, creating non-uniform graphene layers. [75] To guarantee high quality, a high cooling rate should be used. However, the available setup at this stage did not allow such rapid cooling. For this reason, copper, which has a lower carbon solubility (does not exceed 0.02 % even at high temperatures), should present better results despite the slow cooling rate. [76] Furthermore, the oxidation potential of Ni (+0.28 V for Ni^{2+}) is higher than Cu (-0.34 V for Cu^{2+}), which means that Ni is more easily oxidized than Cu, because the more positive the oxidation potential, the greater the tendency of the species to be oxidized. At high temperatures, the oxidation rate of metals increase and, as for the CVD process the metal substrate must be pure, substrates resistant to oxidation are preferable. Therefore, the chosen substrate was Cu. [77]

Among the most popular carbon sources are methane, ethylene and acetylene. Between these three, methane permits the production of high quality and excellent crystallinity monolayer graphene. [78] For this hydrocarbon, a reaction temperature of 1000 °C is sufficient to dissociate methane and produce high quality graphene. At the same time, it is far enough from the melting temperature of the metallic substrates, in particular Cu, for which it is 1085 °C. [73] The carbon source concentration in the gas inlet is a crucial factor for determining the graphene quality and number of layers. To obtain monolayer graphene, a concentration from 10 ppm to 0.2 % (in volume) should be used. [49, 73, 79, 80] A higher number of layers up to 14 layers (MLG) can be obtained by varying the methane concentration between 0.5 % and 10 % (in volume). [71, 81, 82]

It is not clear in the literature which reaction time is best or if it even influences the obtained graphene. However, Nguyen et al. [83] verified that 5 min of CVD reaction was enough to completely cover the Cu surface with graphene and increasing the reaction time will only

influence the graphene quality rather than the number of layers, the optimal time being 30 min. [83] Besides this work, reaction times between 3 and 30 min were reported for the production either of monolayer graphene and MLG, so this was the selected range. [49, 71, 83]

Hydrogen presence is essential because it induces an efficient decomposition of methane on the copper surface and it provides a reduced environment that prevents the oxidation of graphene at high temperatures. However, H_2 may decompose at high temperatures on the Cu surface, recombining with carbon atoms and forming methane in the reverse reaction; this limits the nucleation of graphene layers and may result in etching of the graphene that had already formed. Hence, the final product results from an equilibrium between methane decomposition and graphene etching reactions, in which both CH_4 and H_2 are involved, so the H_2/CH_4 ratio needs to be carefully defined. [74, 82] It was demonstrated that the ideal H_2/CH_4 ratio to produce MLG ranges between 50 and 200, i.e. hydrogen always in excess. [49, 71, 81, 82] As reported by Jun Pu et al. [71], argon flow should be stopped during the reaction step, therefore CH_4 concentration determines the H_2/CH_4 ratio: a CH_4 concentration of 0.5 %, 1 % and 2 % corresponds to a H_2/CH_4 ratio of 200, 100 and 50, respectively. [71] Table 4.6 summarizes the values and ranges defined for each operating condition.

Table 4.6 - Operating conditions values or ranges for the CVD process.

Heating rate	3 °C·min^{-1}
Cooling rate	3 °C·min^{-1}
Pressure of the system	1 atm
Carbon precursor	CH_4
Metallic substrate	Copper deposited on a SiO_2/Si wafer
Reaction time	3 to 30 min
Reaction temperature	1000 °C
Carbon precursor concentration	0.5 % to 2 % (in volume)
Ratio H_2/CH_4	50 to 200

4.2.2 Design of experiments

Even if carefully cleaned, residual oxidizing impurities may remain in the reactor's atmosphere and, as oxidation rate increases with temperature, the oxidation of the Cu surface is inevitable. Since the Cu surface acts as catalyst, it must be as pure as possible. Therefore, a H_2 flow could be introduced before the reaction in order to reduce the oxidized copper and recover a pure metal surface. [84]

For the initial CVD experiments, a reference experiment was defined (experiment 1), according to the best values found in literature, and then several experiments were performed varying the other operating parameters in order to understand their influence. [71] The conditions of the six experiments performed are shown in Table 4.7.

Table 4.7 - Design of experiments.

Experiment		G1	G2	G3	G4	G5	G6
% CH_4		2	2	**0.5**	2	2	**10**
H_2/CH_4		50	50	**200**	50	50	**9**
Reaction time / min		5	5	5	5	**30**	5
Flows / $mL \cdot min^{-1}$							
Heating	Ar	200					
30 min before reaction	Ar	200	**150**	200	200	200	200
	H_2	0	**300**	0	0	0	0
Growth	Ar	0	0	0	**153**	0	0
	H_2	500	500	500	**350**	500	459
	CH_4	10	10	2.5	**7**	10	51
Cooling	Ar	150					

The flows of each gas during the reaction step was defined according to the CH_4 concentration and H_2/CH_4 ratio, taking in account that the total flow should be as close to 510 $ml \cdot min^{-1}$ as possible, so that the total flow was constant and wouldn't influence the results. This value, as well as the flow of Ar and H_2 30 min before the reaction in the second experiment and the Ar flow during cooling, was defined according to Jun Pu et al. article. [71]

To guarantee high quality graphene, the catalyst surface must be as smooth as possible, and so sputtering thin-film deposition was used to deposit a thin copper film on SiO_2/Si wafers with good uniformity, reproducibility and adhesion. [85] Initially, a low-vacuum sputtering (Leica EM ACE200) was used. Then, using these Cu samples, six CVD experiments were run according to Table 4.7. These same samples were then characterized by Raman spectroscopy to assess the presence of graphene/graphite and the quality of the deposited material. However, Raman spectra of the different samples did not correspond to typical spectra for MLG or even graphite. So, to understand the possible reason for the unsuccessful graphene deposition, wafers coated with Cu were taken to AFM to analyze the Cu surface and thus evaluate the Cu catalyst quality. To determine the surface roughness two factors were calculated: R_q and R_a. R_q is the root mean square average of height deviations taken from the mean data plane, while R_a is the arithmetic average of the absolute values of the surface height deviations measured from the mean plane.

[86] AFM results showed a R_q of 5.21 nm and R_a of 4.15 nm, which demonstrate that the growth of uniform graphene layers is very unlikely, since a single-layer graphene thickness is around 0.4 nm and MLG thickness ranges from 1.75 nm (5 layers) to 4 nm (12 layers). [37, 70]

Since the copper surface must be as smooth and compact as possible, a magnetron sputtering equipment was then used. The obtained values for R_q and R_a were 2.36 nm and 1.86 nm, respectively, which are low enough to produce high quality MLG, since a R_q of 1 nm is sufficient to produce single-layer graphene. [37, 70] The thickness of the Cu films was also determined to be 2.25 µm (by AFM and then validated with SEM). Thus, this deposition technique was used for the following depositions. Images from AFM of the Cu surface are shown in Figure 4.6.

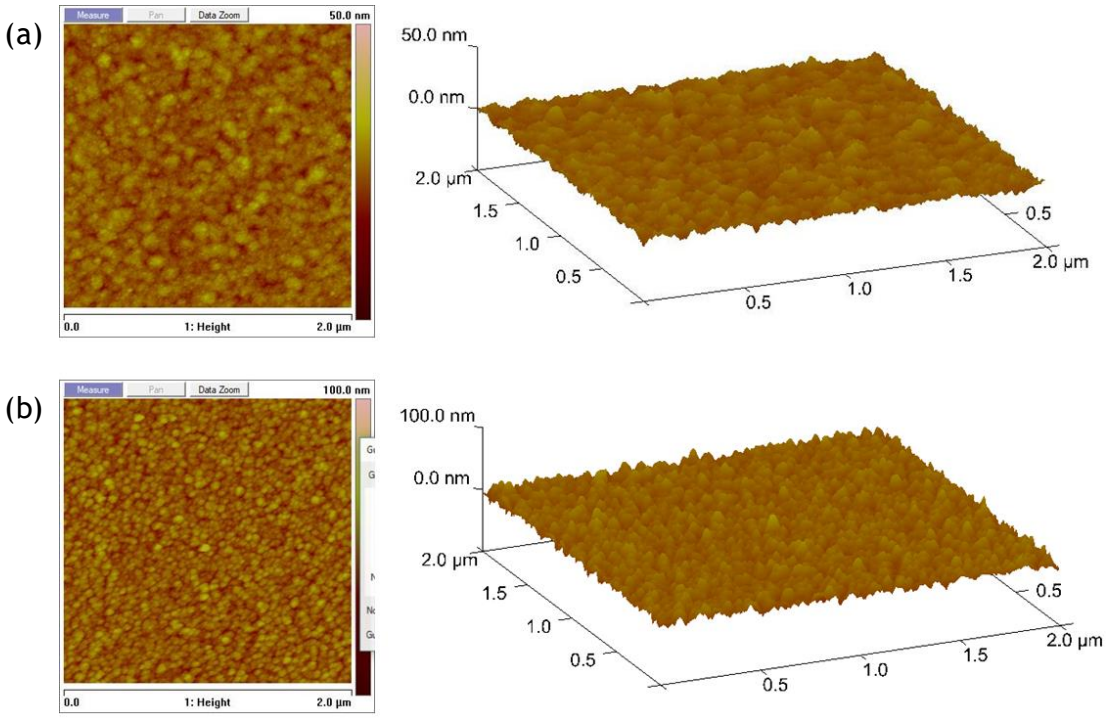

Figure 4.6 - AFM surface characterization in 2D and 3D for the copper deposited by (a) magnetron sputtering and (b) low-vacuum sputtering on a silicon wafer.

The Copper surface morphology was analysed by SEM - Figure 4.7, which revealed a flat surface with a black dot pattern. About the Copper structure, it must be nanocrystalline, presenting grains with average pore diameter inferior to 100 nm, which frontiers are not perceptible by Figure 4.7. An Energy Dispersive X-Ray Diffractometer was realized at the grey background and the black dots, showing an irrelevant Cu weigth concentration difference of 4 % between both spots (93 % for the grey background and 98 % for the black dot). These black spots could be imperfections, such as pores, caused by the sputtering depostion.

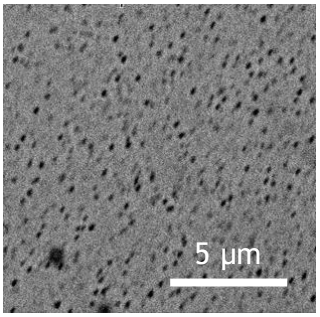

Figure 4.7 - SEM image of the morphology of copper deposited by magnetron sputtering on a Si/SiO_2 wafer.

Cu samples were deposited by the new sputtering equipment and according to the design of experiments - Table 4.7 Raman spectroscopy was again used to evaluate the presence and quality of the CVD product. However, no graphene peak was observed and only peaks at 290 cm^{-1}, 340 cm^{-1} and 630 cm^{-1} appeared, which correspond to tenorite, a copper oxide mineral with formula CuO - Figure 4.8(a). This observation lead to suspect that oxidation of the copper surface was occurring during the experiments. To further confirm that the copper substrate was indeed oxidized, XRD analyses were performed – Figure 4.8(b In the XRD diffractogram, peaks at 29.6°, 36.6°, 42.5° and 51.4° correspond to Cuprite (CuO_2), at 32.6°, 35.6°, 38.8°, 46.5°, 49.0°, 53.7° and 58.5° correspond to CuO, and only the peak at 43.3° correspond to Cu; this specific peak of Cu only appears in the sample (G1) that was subjected to H_2 flow 30 min before reaction. [87] This last peak proves that H_2 does reduces the oxidized Cu. The area below the XRD peaks from CuO_2 is smaller than the ones from CuO, and there is no visible peak at in the Raman spectrum for CuO_2 (at 220 cm^{-1}, 410 cm^{-1} and 630 cm^{-1}), probably because they were hindered by the peaks of CuO. [87] Furthermore, CuO is dark-grey while CuO_2 is dark-red, and all sampes became grey after the CVD deposition. Therefore, it was concluded that most of the copper oxide formed was CuO. This oxidized surface was responsible for the lack of graphene growth, since Cu catalyses the reaction and, if it oxidises, methane cannot decompose into graphene layers. Therefore, it was perceived that the cleaning procedure (200 $mL \cdot min^{-1}$ of Ar during the heating time) was not being effective in eliminating the oxidizing impurities from inside the tube (essentially oxygen).

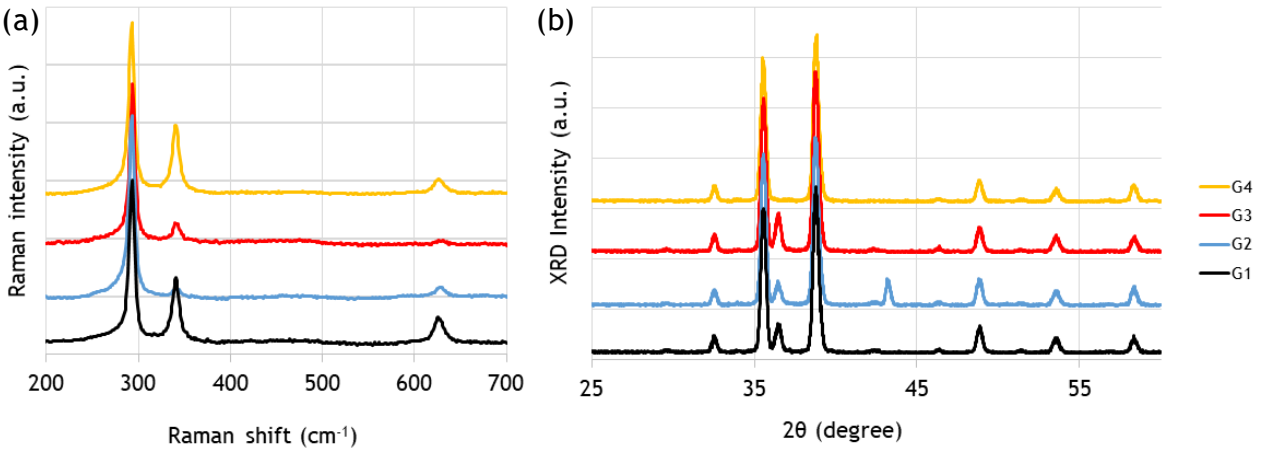

Figure 4.8 - (a) Raman spectra and (b) XRD diffractograms of the first four experiments.

4.2.3 Purge optimization

Considering the dimensions of the quartz tube and an Ar flow of 200 $mL \cdot min^{-1}$, the Reynolds number is 3540, which means that the flow regime is transitional (2100 > Reynolds > 4000) and stagnant volumes of air likely exist at the tube entrance. [88] Figure 4.9 is a Computational Fluid Dynamics (CFD) simulation showing the contours of velocity magnitude in a similar flow,

and it allows us to perceive the formation of the stagnant volumes (blue color). Thus, oxidizing impurities remain in these volumes even after the argon purge, and diffuse into the Cu films during the CVD procedure, oxidizing their surface. As oxidation rates increase with temperature, even vestigial amounts of oxygen would be enough to oxidize the Cu surface, and therefore its concentration inside the tube must be as low as possible from the beginning of the experiment.

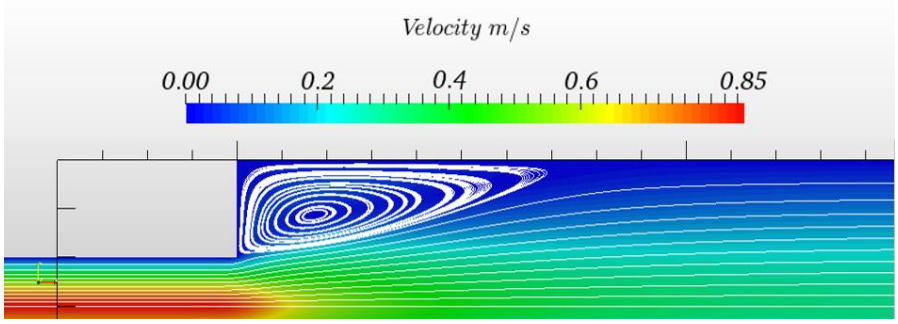

Figure 4.9 - *Computational Fluid Dynamics simulation of the velocity contours in a symmetrical system similar to the one of this study.*

To solve this problem, high flow short time pulses with low flow intervals were introduced into the tube to create turbulence inside it and thus inhibit the formation of stagnant volumes. In order to find the best cleaning procedure, several tests were made varying the number, duration, and Argon flow of these cleaning pulses. Figure 4.10 shows pictures of copper samples submited to high temperatures using diferent cleaning procedures.

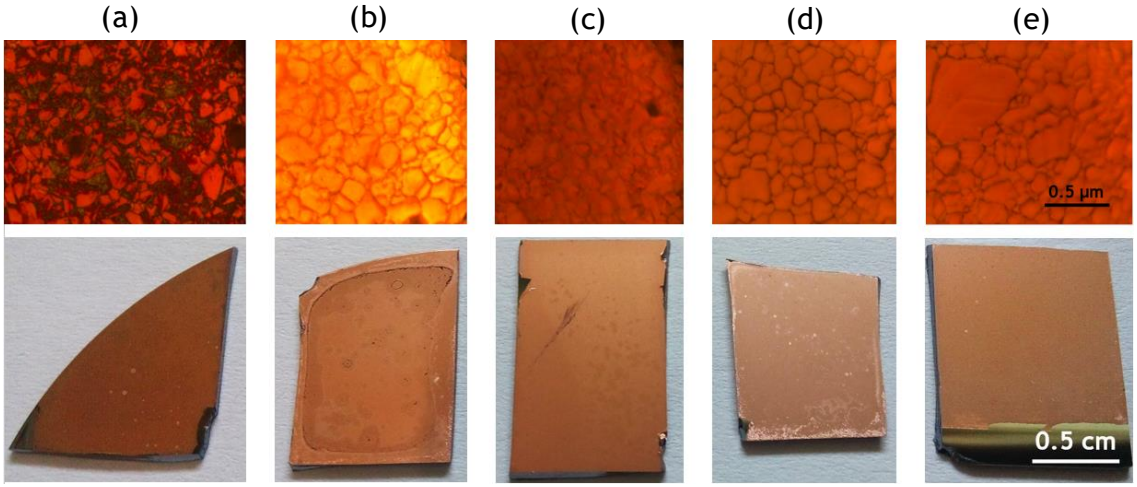

Figure 4.10 - Cu substrates after heating until 1000 ^{0}C and cooling to room temperature at 3 ^{0}C·min^{-1} under 200 L·min^{-1} of Ar flow, with different cleaning strategies: (a) without cleaning pulses at the beginning, (b) without cleaning pulses at the beginning and with 150 mL·min^{-1} of Ar and 300 mL·min^{-1} of H_2 30 min before the reaction, (c) with cleaning pulses at the beginning, (d) with cleaning pulses at the beginning and with 150 mL·min^{-1} of Ar and 300 mL·min^{-1} of H_2 30 min before the reaction and (e) optimized cleaning pulses with 150 mL·min^{-1} of Ar and 300 mL·min^{-1} of H_2 30 min before the reaction. Above are images taken by the optical microscope integrated in the Raman equipment and below are pictures of the correspondent above samples.

An oxygen analyzer (AMETEK CG1000) was used to determine the oxygen concentration after each cleaning procedure and to confirm that 0 ppm had been reached. The optimum procedure found so far was six pulses of 1.5 $L \cdot min^{-1}$ of Argon during 1 min, followed by 300 $mL \cdot min^{-1}$ during 5 min. At 1.5 $L \cdot min^{-1}$ the Reynolds value is 26557, which guarantees turbulent regime (Reynolds > 4000). [88] Another possible solution to reach the stagnant volumes is to invert the flow direction during the cleaning procedure or to place a small object near the tube entrance to redirect the intake flow to the stagnant volumes.

The optical microscope pictures shows that the copper heated to 1000 °C presents large and well-defined grains. This was expected to occur since the Cu film is subjected to temperatures higher than its recrystallization temperature (120 °C) for more than 10 h during the oven heating and cooling, what causes recrystallization and grain growth. [89] However, the grains are not favorable to monolayer graphene growth, because their boundaries usually have much higher chemical activation energy than those of the flat regions of Cu and methane tend to decompose on higher chemical activation energy sites. Thus, the grain boundaries act as nucleation sites for multilayer growth. [90] The slow heating rate used in this study could be advantageous in this context, since the grain size increases and, consequently, the boundary density decreases with time, and copper is submitted to temperatures above 120 °C during 5 h before the reaction. Still, these boundaries are not that favorable for this study, since the intended product is MLG.

By Figure 4.10 it is possible to conclude that the cleaning pulses allowed the surface to be more uniform (comparing (b) with (d) and (e)) and that the H_2 feed for 30 minutes before CVD reaction made the surface brighter (comparing (a) with (b) and (c) with (d)). This indicates that hydrogen reduced part of the copper oxide that was already formed since the reflectance for copper and copper oxide are, respectively, 0.82 and 0.20 at a wavelength of 600 nm. [91, 92]. Nevertheless, the Cu surface lost its brightness during the procedure (comparing (e) Figure 3.5), fact that should be related with the grain size increase and consequence increase of roughness of the Cu surface after the slow heating and cooling.

A third set of six experiments was done with the optimized cleaning pulses, but again the Raman and XRD results demonstrated that no MLG was produced. The Figure 4.11 shows the XRD diffractrogram from the Cu sample deposited by magnetron sputtering (black), from the Cu substrate after the reference experience with (red) and without (blue) the reaction step.

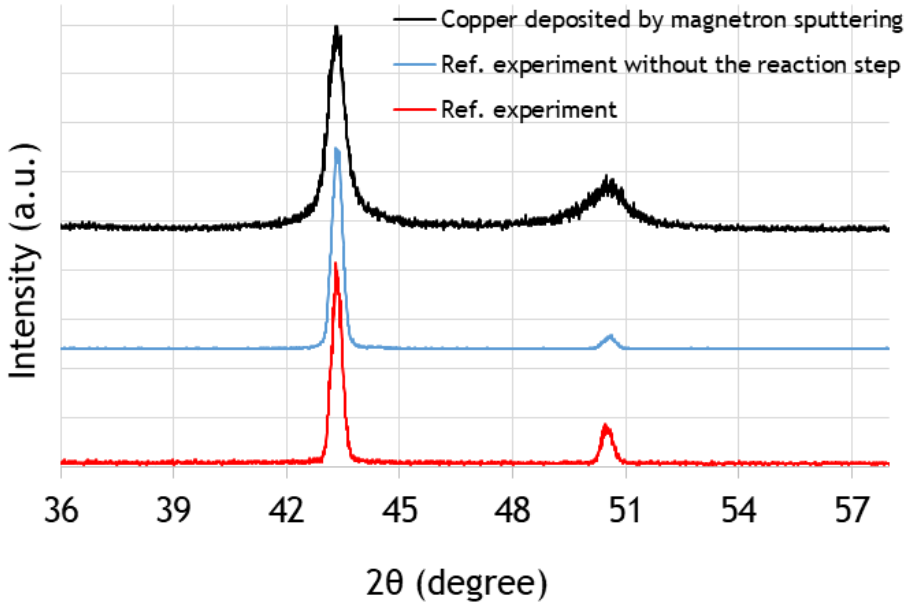

Figure 4.11 – XRD diffractograms for copper deposited by magnetron sputtering on a SiO_2 and for the substrate after the realization of the reference graphene production experiment whit and without the reaction step.

All the XRD diffractograms only presents peaks assigned to copper (located at 43.3º and 50.5º), which validates the cleaning procedure. Furthermore, XRD diffractograms also validate the nanocrystallinity of the copper deposited by magnetron sputtering, because XRD peaks from nanocrystals have low definition and large width when compared with large grains, i.e. grains after annealing, which is verified in the diffractograms. However, X-ray diffractogram of the graphene growth experiment doesn't present the peak characteristic of graphene, which means that no graphene was produced.

This could have occurred because the hydrogen concentration that still remains inside the tube immediately after the reaction step is higher than its initial concentration (H_2 is a product of the CH_4 decomposition) and it reacts with the produced graphene, creating methane in the reverse reaction, destroying the graphene layer. As the cooling rate is very low, the temperature is kept high inside the tube for a long time, which ensures enough energy for the etching reaction, leading to the total destruction of the graphene layer. It is well-known that a reaction product state achieved at high temperatures can degrade or change to a lower energy state, in a spontaneous reaction, because every system evolves in the direction of the minimum free energy to reach a more stable state, by increasing entropy or decreasing enthalpy. Thus, it is essential to have a very fast, almost instantaneous, cooling to room temperature to conserve the high temperature state of graphene.

5 Conclusion

Carbon papers have proven to be a very promising back-contact for PSCs. Initially, two adhesion layers were selected (PEDOT:PSS and spiroOMeTAD) for an efficient integration of the carbon paper into the final device. It was concluded that spiroOMeTAD has less affinity to the carbon paper and so lower photovoltaic performance results were achieved (maximum efficiency of 3.30 %). Regarding PEDOT:PSS, two different additives were considered for improving its properties and the deposition uniformity but none resulted in enhanced photovoltaic performance of the final devices: best efficiency of 6.91 % for bare PEDOT:PSS, 6.25 % for PEDOT:PSS with isopropanol and 5.55 % for PEDOT:PSS with *D*-sorbitol. *D*-sorbitol, despite improving the interface bonding between the adhesion layer and the HTM, failed at improving conductivity and stability of the solution, but this might be further improved by optimizing its concentration and curing procedure. Adding isopropanol to allow the deposition of PEDOT:PSS by spin-coating showed several advantages, such as ensuring greater uniformity of the capping layer of the adhesion layer (because it allows spincoating deposition) and greater probability of total filling of pores (because it makes the solution more hydrophobic). However, due to PEDOT:PSS dilution, its properties may be compromised, and it could be partially thrown out during the spin, diminishing the photovoltaic performance of the final device.

Two types of carbon papers were used for studying their structural and electrical properties' influence on the solar cell performance. By comparing the results, it was concluded that an overall improved power conversion efficiency of the solar cell is achieved for the paper with smaller pore diameter, as it results in an increased interfacial contact (where the charge carriers recombination occurs) and so in a reduced interfacial resistivity.

A complete analysis of the photovoltaic performance parameters (I_{sc}, V_{oc} and *FF*) was performed for each adhesion layer and it was verified that the I_{sc} decrease was the main responsible for the lower efficiencies (loss of 28 % and 58 % for the PEDOT:PSS and spiroOMeTAD best cells, respectively). These losses are caused by electron extraction constraints in the back-contact, which, in this case, is doubly limited: by the interface of the adhesion layer with the HTM and by the interface of the adhesion layer with the carbon paper.

This initial work concerning the deposition of graphene by CVD permitted a better understanding of how each operating condition influences the CVD process and thus allowed for modifications to the existing experimental setup. The decision to produce multilayer graphene rather than few-layer graphene was made because its sheet resistance is about 60 % smaller, and the decrease in transparency is not significant (about 7 %). After selecting adequate operating conditions and range of experimental variables for optimization purposes, it was noted that rapid quenching after CVD reaction is indispensable to preserve the graphene

quality produced at high temperatures. It was also concluded that it is mandatory to ensure a fully inert atmosphere within the reaction tube to prevent catalyst oxidation, and to guarantee a sufficiently smooth catalyst surface (R_q < 2.5 nm). Both optimizations were performed and adequate procedures defined. Thus, for the copper substrates, magnetron sputtering deposition can be used for producing the above mentioned surface roughness; for the optimization of the purge step, a procedure of short time high flow Argon pulses (1 min for 1.5 $L \cdot min^{-1}$) with long time periods of Argon at a low flow rate (5 min for 300 $mL \cdot min^{-1}$) should be implemented before heating.

6 Assessment of the work done

6.1 Objectives Achieved

Regarding the carbon papers work, the majority of objectives were reached. The forecast tasks envisaged: selection of appropriate adhesion layers, use of two different carbon papers in order to understand the properties that influence device performance, optimization of the deposition of adhesion layers, optimization of carbon paper integration into complete devices, assembly and characterization of complete PSC devices. Two tasks need further optimization: the deposition of adhesion layers and the carbon paper integration into complete devices. Nevertheless, this study was of fundamental importance to identify the main experimental limitations in reaching good interfacial contacts and to give the appropriate tips for overcoming them. Moreover, an overall power conversion efficiency with a carbon material as back-contact of almost 7 % in such an innovative approach may predict that a PCE of 10 % could be reached very soon.

Looking at graphene deposition by CVD work, the forecasted tasks were: assembling/adapting an experimental setup for CVD deposition technique, literature review concerning the influence of the main operating conditions, design of experiments taking into account the state of the art, characterization of graphene/graphite material growth by CVD. For this study only the first two tasks were totally fulfilled. Unfortunately, the low cooling rate did not allow for a carbon-based material to be obtained by CVD. Nevertheless, this study was of great importance in identifying the modifications needed in the experimental setup as well as allowing the definition of correct protocols to perform the CVD experiments.

6.2 Limitations and Future Work

The major limitation in both studies (carbon papers and graphene) that prevent them from fully reaching the forecasted objectives was the time spent in each set of experiments. In the case of the carbon papers work, the most time-consuming procedure was the fabrication of solar cells. Besides taking around three days for assembly and another day for characterization of a batch of maximum 8 cells, all steps of the fabrication process are very meticulous, which prevented parallel activities. In the case of graphene growth, the oven took approximately 5 and a half hours to warm up and approximately 7 hours to cool down to room temperature, i.e. each CVD test took one day to complete. So, to carry out the 6 predefined experiments, seven working days were necessary. Then, the characterization of the samples was performed in an external institution with the need of advance booking.

Another limitation identified was the need to optimize the deposition process of copper, which was not initially forecasted.

As future work, the roughness of the Cu samples after annealing could be determined by AFM, to determine the true roughness at the reaction step, because this could also be a limiting factor for the growth of high-quality graphene. Furthermore, it is essential to modify the cooling rate of the CVD deposition procedure to allow the cooling to be almost instantaneous. This will favor graphene growth and also diminish the time of the experiments. For that, the oven should have a chiller or an opening system, to allow the tube to be directly exposed to room temperature, to increase the cooling rate. Instead, a mechanism can be implemented to move the samples from the center of the furnace (where the resistances are) to the end of the tube, which is not covered by the oven. Upon cooling, it is essential to not expose the sample to the ambient atmosphere until the temperature drops to approximately 150 °C to prevent the sample from oxidizing.

In addition, the tube can also be exchanged by another with a smaller diameter as it does not compromise the tests and decreases the gas consumption. On the other hand, a tube with a larger diameter would allow the study of graphene production on a larger scale, which is an equally interesting topic to be studied.

With the high cooling rate guaranteed, Ni can also be tested as a catalyst, since it allows lower reaction temperatures (less energy consumption) and it is more resistant to recrystallization than Cu (Ni recrystallization temperature is 370 °C while for Cu is 120 °C). Very promising preliminary results with Ni were obtained (not presented in this thesis because there were only two experiments without further optimization), allowing the growth of thick graphite. Instead of replacing the catalyst, Cu may also be used in another form. Since the thickness of the Cu film does not influence the final product, 25 µm Cu sheets (with enough smoothness for the production of high quality graphene) could also be used to facilitate handling, simplify the overall process and eliminate costs associated with sputtering deposition.

Aiming to reduce costs and time, the tube cleaning by pulses can be optimized through Computational Fluid Dynamics software in order to achieve the same oxygen concentration (< 0 ppm) at the lowest possible cost (i.e. minimum volume of Argon) and time. All variables were optimized for MLG, however, it is also possible to adjust them so that the final product is monolayer graphene, in order to maximize its transparency.

For carbon papers, the limitations and respective actions that can be taken to overcome them were already discussed by the end of Chapter 4.1, Table 4.5.

6.3 Final Assessment

The initial thesis proposal workplan was ambitious and risky. On one hand, there were no previous works reporting the use of carbon papers in perovskite solar cells and so it might not have worked. On the other hand, it was known that implementing a new technique for deposition of a material such as graphene may face several experimental limitations from the very beginning. Nevertheless, carbon papers as back-contact for perovskite solar cells provided very promising results in these first attempts. Despite these initial good results, there are still factors to be further investigated and optimized. In particular, the most relevant modifications to be performed were discussed within this thesis. Then, the first experiments aiming to produce graphene by CVD performed within this thesis work faced several initial constraints that prevented fully reaching the forecasted objectives (waiting time for the catalyst's and other reactants' delivery, length of time of each experiment, characterization techniques' booking service). Although it was not possible to produce graphene, the optimization of the whole process led to a detailed understanding of each variable's influence in the CVD process and allowed the definition of adequate procedures for succeeding in graphene deposition in the very near future.

7 References

1. *BP Statistical Review of World Energy 2017*. 2017.
2. Panwar, N.L., S.C. Kaushik, and S. Kothari, *Role of renewable energy sources in environmental protection: A review.* Renewable and Sustainable Energy Reviews, 2011. **15**(3): p. 1513-1524.
3. Madsen, M.V. *Solar cells - the three generations*. Solar Cells; Available from: http://plasticphotovoltaics.org/lc/lc-solarcells/lc-introduction.html#fn1.
4. NREL, *Best Research-cell Efficiencies*. 2018.
5. Correa-Baena, J.P., et al., *The rapid evolution of highly efficient perovskite solar cells.* Energy and Environmental Science, 2017. **10**(3): p. 710-727.
6. Yu Cai, L.L., Peng Gao, *Promise of Commercialization: Carbon Materials for Low-Cost Perovskite Solar Cells.* 2017.
7. Wonbong Choi, I.L., Raghunandan Seelaboyina, Yong Soo Kang, *Synthesis of Graphene and Its Applications: A Review.* Critical Reviews in Solid State and Materials Sciences, 2010.
8. *LEPABE - Laboratory for Process Engineering, Environment, Biotechnology and Energy* Available from: http://lepabe.fe.up.pt/.
9. Weber, D., *CH3NH3PbX3, ein Pb(II)-System mit kubischer Perowskitstruktur / CH3NH3PbX3, a Pb(II)-System with Cubic Perovskite Structure*, in *Zeitschrift für Naturforschung B*. 1978. p. 1443.
10. Ossila. *Perovskites and Perovskite Solar Cells: An Introduction*. 2017; Available from: https://www.ossila.com/pages/perovskites-and-perovskite-solar-cells-an-introduction.
11. Green, M.A. and A. Ho-Baillie, *Perovskite Solar Cells: The Birth of a New Era in Photovoltaics.* ACS Energy Letters, 2017. **2**(4): p. 822-830.
12. Park, N.-G., *Perovskite solar cells: an emerging photovoltaic technology.* Materials Today, 2015. **18**(2): p. 65-72.
13. Rini, M., et al., *Control of the electronic phase of a manganite by mode-selective vibrational excitation.* Nature, 2007. **449**: p. 72.
14. Kojima, A., et al., *Organometal Halide Perovskites as Visible-Light Sensitizers for Photovoltaic Cells.* Journal of the American Chemical Society, 2009. **131**(17): p. 6050-6051.
15. Razza, S., et al., *Research Update: Large-area deposition, coating, printing, and processing techniques for the upscaling of perovskite solar cell technology.* APL Materials, 2016. **4**(9): p. 091508.
16. Cui, D., et al., *Color-Tuned Perovskite Films Prepared for Efficient Solar Cell Applications.* The Journal of Physical Chemistry C, 2016. **120**(1): p. 42-47.
17. Arora, N., et al., *Perovskite solar cells with CuSCN hole extraction layers yield stabilized efficiencies greater than 20%.* Science, 2017. **358**(6364): p. 768-771.
18. Mesquita, I., L. Andrade, and A. Mendes, *Perovskite solar cells: Materials, configurations and stability.* Renewable and Sustainable Energy Reviews, 2018. **82**: p. 2471-2489.
19. Lee, M.M., et al., *Efficient Hybrid Solar Cells Based on Meso-Superstructured Organometal Halide Perovskites.* Science, 2012. **338**(6107): p. 643-647.
20. Shockley, W. and H.J. Queisser, *Detailed Balance Limit of Efficiency of p-n Junction Solar Cells.* Journal of Applied Physics, 1961. **32**(3): p. 510-519.
21. Marinova, N., S. Valero, and J.L. Delgado, *Organic and perovskite solar cells: Working principles, materials and interfaces.* Journal of Colloid and Interface Science, 2017. **488**: p. 373-389.
22. Salim, T., et al., *Perovskite-based solar cells: impact of morphology and device architecture on device performance.* Journal of Materials Chemistry A, 2015. **3**(17): p. 8943-8969.
23. Domanski, K., et al., *Not All That Glitters Is Gold: Metal-Migration-Induced Degradation in Perovskite Solar Cells.* ACS Nano, 2016. **10**(6): p. 6306-6314.
24. Wojciechowski, K., et al., *Sub-150 [degree]C processed meso-superstructured perovskite solar cells with enhanced efficiency.* Energy & Environmental Science, 2014. **7**(3): p. 1142-1147.
25. Anaraki, E.H., et al., *Highly efficient and stable planar perovskite solar cells by solution-processed tin oxide.* Energy & Environmental Science, 2016. **9**(10): p. 3128-3134.

26. Xiong, Y., et al., *Fully printable hole-conductor-free mesoscopic perovskite solar cells based on mesoporous anatase single crystals.* New Journal of Chemistry, 2018. **42**(4): p. 2669-2674.
27. Ye, S., et al., *A Breakthrough Efficiency of 19.9% Obtained in Inverted Perovskite Solar Cells by Using an Efficient Trap State Passivator Cu(thiourea)I.* Journal of the American Chemical Society, 2017. **139**(22): p. 7504-7512.
28. Lang, F., et al., *Influence of Radiation on the Properties and the Stability of Hybrid Perovskites.* Advanced Materials, 2018. **30**(3): p. 1702905-n/a.
29. Yang, S., et al., *Recent advances in perovskite solar cells: efficiency, stability and lead-free perovskite.* Journal of Materials Chemistry A, 2017. **5**(23): p. 11462-11482.
30. Mahdi, T.M., et al., *Large-Grain Tin-Rich Perovskite Films for Efficient Solar Cells via Metal Alloying Technique.* Advanced Materials, 2018. **30**(11): p. 1705998.
31. Leijtens, T., et al., *Overcoming ultraviolet light instability of sensitized TiO2 with meso-superstructured organometal tri-halide perovskite solar cells.* Nature Communications, 2013. **4**: p. 2885.
32. Wang, J.X., et al., *Progress of new carbon material research in perovskite solar cells.* Wuli Xuebao/Acta Physica Sinica, 2016. **65**(5).
33. McCreery, R.L., *Advanced Carbon Electrode Materials for Molecular Electrochemistry.* Chemical Reviews, 2008. **108**(7): p. 2646-2687.
34. Fuente, J.d.L. *Graphene - What Is It?* ; Available from: https://www.graphenea.com/pages/graphene#.WoW-5qhl_IU.
35. Hashmi, S.G., et al., *High performance carbon-based printed perovskite solar cells with humidity assisted thermal treatment.* Journal of Materials Chemistry A, 2017. **5**(24): p. 12060-12067.
36. Lim, E.L., et al., *A Mini Review: Can Graphene Be a Novel Material for Perovskite Solar Cell Applications?* Nano-Micro Letters, 2018. **10**(2).
37. Soldano, C., A. Mahmood, and E. Dujardin, *Production, properties and potential of graphene.* Carbon, 2010. **48**(8): p. 2127-2150.
38. *Monolayer Graphene on SiO_2/Si*, Graphenea, Editor. 2018.
39. Bolotin, K.I., et al., *Ultrahigh electron mobility in suspended graphene.* Solid State Communications, 2008. **146**(9): p. 351-355.
40. Earth, F.C. *Carbon paper: AvCarb - MGL*. 2018; Available from: https://www.fuelcellearth.com/product-category/carbon-paper/avcarb-mgl/.
41. Zamel, N., *Transport Properties of the Gas Diffusion Layer of PEM Fuel Cells*. 2011, UWSpace.
42. Bouclé, J. and N. Herlin-Boime, *The benefits of graphene for hybrid perovskite solar cells.* Synthetic Metals, 2016. **222**: p. 3-16.
43. Nobelprize.org. *About the Nobel Prize in Physics 2010 - press release*. 2010; Available from: https://www.nobelprize.org/nobel_prizes/physics/laureates/2010/press.html.
44. Jacob Tse-Wei Wang, J.M.B., Eva M. Barea, Antonio Abate, Jack A. Alexander-Webber, Jian Huang, Michael Saliba, Iván Mora-Sero, Juan Bisquert, Henry J. Snaith, and Robin J. Nicholas, *Low-Temperature Processed Electron Collection Layers of Graphene/TiO2 Nanocomposites in Thin Film Perovskite Solar Cells.* Nano Letters, 2013. **14**(2): p. 724-730.
45. Yan K, W.Z., Li J, Chen H, Yi Y, Zheng X, Long X, Wang Z, Wang J, Xu J, Yang S., *High-performance graphene-based hole conductor-free perovskite solar cells: Schottky junction enhanced hole extraction and electron blocking*. Small, 2015.
46. You P, L.Z., Tai Q, Liu S, Yan F, *Efficient Semitransparent Perovskite Solar Cells with Graphene Electrodes.* Advanced materials, 2015. **27**(24): p. 3632-8.
47. Wei, W., et al., *Potassium-chemical synthesis of 3D graphene from CO2 and its excellent performance in HTM-free perovskite solar cells.* Journal of Materials Chemistry A, 2017. **5**(17): p. 7749-7752.
48. Valverde, J.L., *The Transfer of Graphene: A Review.* Bulgarian Journal of Physics, 2016. **43**(2): p. 121–147.
49. Bhaviripudi, S., et al., *Role of Kinetic Factors in Chemical Vapor Deposition Synthesis of uniform Large Area Graphene Using Copper Catalyst.* Nano Letters, 2010. **10**(10): p. 4128-4133.

50. Lavin-Lopez, M.P., et al., *CVD-graphene growth on different polycrystalline transition metals.* AIMS Materials Science, 2017. **4**(1): p. 194-208.
51. Zhang, Y., et al., *Comparison of Graphene Growth on Single-Crystalline and Polycrystalline Ni by Chemical Vapor Deposition.* The Journal of Physical Chemistry Letters, 2010. **1**(20): p. 3101-3107.
52. Li, X., et al., *Evolution of Graphene Growth on Ni and Cu by Carbon Isotope Labeling.* Nano Letters, 2009. **9**(12): p. 4268-4272.
53. Jang, J., et al., *Low-temperature-grown continuous graphene films from benzene by chemical vapor deposition at ambient pressure.* Scientific Reports, 2015. **5**: p. 17955.
54. Michael Saliba, T.M., Ji-Youn Seo, Konrad Domanski, Juan-Pablo Correa-Baena, Mohammad Khaja Nazeeruddin, Shaik M. Zakeeruddin, Wolfgang Tress, Antonio Abate, Anders Hagfeldtd and Michael Gratzel, *Cesium-containing triple cation perovskite solar cells: improved stability, reproducibility and high efficiency.* Energy & Environmental Science, 2016. **9**.
55. Wall, M., *The Raman Spectroscopy of Graphene and the Determination of Layer Thickness.* Thermo Fisher Scientific, 2011.
56. *UHV Kelvin Probe Manual 2017*. Converting A Contact potencial difference measurement to work function, ed. KPTechnology. 2017.
57. Leijtens, T., et al., *Hole Transport Materials with Low Glass Transition Temperatures and High Solubility for Application in Solid-State Dye-Sensitized Solar Cells.* ACS Nano, 2012. **6**(2): p. 1455-1462.
58. J., S.H. and G. M., *Electron and Hole Transport through Mesoporous TiO2 Infiltrated with Spiro-MeOTAD.* Advanced Materials, 2007. **19**(21): p. 3643-3647.
59. Nardes, A.M., et al., *Conductivity, work function, and environmental stability of PEDOT:PSS thin films treated with sorbitol.* Organic Electronics, 2008. **9**(5): p. 727-734.
60. Rutledge, S.A. and A.S. Helmy, *Carrier mobility enhancement in poly(3,4-ethylenedioxythiophene)-poly(styrenesulfonate) having undergone rapid thermal annealing.* Journal of Applied Physics, 2013. **114**(13): p. 133708.
61. Rudiger Schwelss, C.M., Tanja Damjanovic, Ivano Gaibati, Nico Haak, *SIGRACET® Gas Diffusion Layers for PEM Fuel Cells, Electrolyzers and Batteries*, S.G.-T.C. Company, Editor. 2018.
62. Helmenstine, A.M. *Flow of Electric Current Through Materials*. Table of Electrical Resistivity and Conductivity 2018; Available from: https://www.thoughtco.com/table-of-electrical-resistivity-conductivity-608499.
63. El-kharouf, A., et al., *Ex-situ characterisation of gas diffusion layers for proton exchange membrane fuel cells.* Journal of Power Sources, 2012. **218**: p. 393-404.
64. Sproul, A., *Understanding the p-n Junction*. Solar Cells: Resource for the Secondary Science Teacher. 2003.
65. Elumalai, N.K. and A. Uddin, *Open circuit voltage of organic solar cells: an in-depth review.* Energy & Environmental Science, 2016. **9**(2): p. 391-410.
66. *Solar Cells: A Guide to Theory and Measurement*. 2017; Available from: https://www.ossila.com/pages/solar-cells-theory.
67. Honsberg, C. and S. Bowden. *Short-Circuit Current*. Solar Cell Operation 2018; Available from: https://www.pveducation.org/pvcdrom/short-circuit-current.
68. Shi, Y. and X. Dong, *The factors influencing nonlinear characteristics of the short-circuit current in dye-sensitized solar cells investigated by a numerical model.* Chemphyschem, 2013. **14**(9): p. 1985-92.
69. Leenaerts, O., et al., *The work function of few-layer graphene.* Journal of Physics: Condensed Matter, 2017. **29**(3): p. 035003.
70. Singh, A., et al., *Estimation of intrinsic work function of multilayer graphene by probing with electrostatic force microscopy.* Applied Surface Science, 2017. **402**: p. 271-276.
71. Pu, J., et al., *Chemical vapor deposition growth of few-layer graphene for transparent conductive films.* RSC Advances, 2015. **5**(55): p. 44142-44148.
72. Kosuke, N., et al., *Mobility Variations in Mono- and Multi-Layer Graphene Films.* Applied Physics Express, 2009. **2**(2): p. 025003.

73. Vlassiouk, I., et al., *Large scale atmospheric pressure chemical vapor deposition of graphene.* Carbon, 2013. **54**: p. 58-67.
74. Ghoneim, M.T., *Efficient Transfer of Graphene –Physical and Electrical Performance Perspective*. 2012, King Abdullah University of Science and Technology.
75. Shelton, J.C., H.R. Patil, and J.M. Blakely, *Equilibrium segregation of carbon to a nickel (111) surface: A surface phase transition.* Surface Science, 1974. **43**(2): p. 493-520.
76. Ellis, D.E., et al., *Interstitial carbon in copper: Electronic and mechanical properties.* Philosophical Magazine B, 1999. **79**(10): p. 1615-1630.
77. Brown, T., LeMay, H., Bursten, B., Murphy, C., Woodward, P., *Electrochemistry*, in *CHEMISTRY - The central science*. 2012: USA.
78. H. Cheun Lee, W.-W.L., Siang-Piao Chai, Abdul Rahman Mohamed, Azizan Aziz, Cheng-Seong Khe, N. M. S. Hidayaha, U. Hashima *Review of the synthesis, transfer, characterization and growth mechanisms of single and multilayer graphene.* RSD Advances, 2017(26).
79. Trinsoutrot, P., et al., *High quality graphene synthesized by atmospheric pressure CVD on copper foil.* Surface and Coatings Technology, 2013. **230**: p. 87-92.
80. Wei, W., et al., *Control of thickness uniformity and grain size in graphene films for transparent conductive electrodes.* Nanotechnology, 2012. **23**(3): p. 035603.
81. Yao, Y., et al., *Controlled Growth of Multilayer, Few-Layer, and Single-Layer Graphene on Metal Substrates.* The Journal of Physical Chemistry C, 2011. **115**(13): p. 5232-5238.
82. Kostogrud, I.A., K.V. Trusov, and D.V. Smovzh, *Influence of Gas Mixture and Temperature on AP-CVD Synthesis of Graphene on Copper Foil.* Advanced Materials Interfaces, 2016. **3**(8): p. 1500823-n/a.
83. Nguyen, V.T., et al., *Synthesis of multi-layer graphene films on copper tape by atmospheric pressure chemical vapor deposition method.* Advances in Natural Sciences: Nanoscience and Nanotechnology, 2013. **4**(3).
84. Reckinger, N., et al., *The influence of residual oxidizing impurities on the synthesis of graphene by atmospheric pressure chemical vapor deposition.* Carbon, 2013. **63**: p. 84-91.
85. *Advantages of Sputter Technology*, S. Glass, Editor. 2015.
86. De Oliveira, R.R.L., et al., *Measurement of the Nanoscale Roughness by Atomic Force Microscopy: Basic Principles and Applications*. 2012.
87. RRUFF™, *Search RRUFF Sample Data*.
88. Joseph Smith Jr, M.C. *Reynolds Number & Pipe Flow*. 2002; Available from: https://ocw.mit.edu/courses/mechanical-engineering/2-000-how-and-why-machines-work-spring-2002/study-materials/TurbulentFlow.pdf.
89. William D. Callister, J., *Dislocations and Strengthening Mechanisms* in *Materials Science and Engineering - An Introduction*. 2007, John Wiley & Sons, Inc.
90. Liu, W., et al., *Synthesis of high-quality monolayer and bilayer graphene on copper using chemical vapor deposition.* Carbon, 2011. **49**(13): p. 4122-4130.
91. Wieder, H. and A.W. Czanderna, *Optical Properties of Copper Oxide Films.* Journal of Applied Physics, 1966. **37**(1): p. 184-187.
92. Johnson, P.B. and R.W. Christy, *Optical Constants of the Noble Metals.* Physical Review B, 1972. **6**(12): p. 4370-4379.

Appendix 1 Solar cell efficiency improvement throughout the years

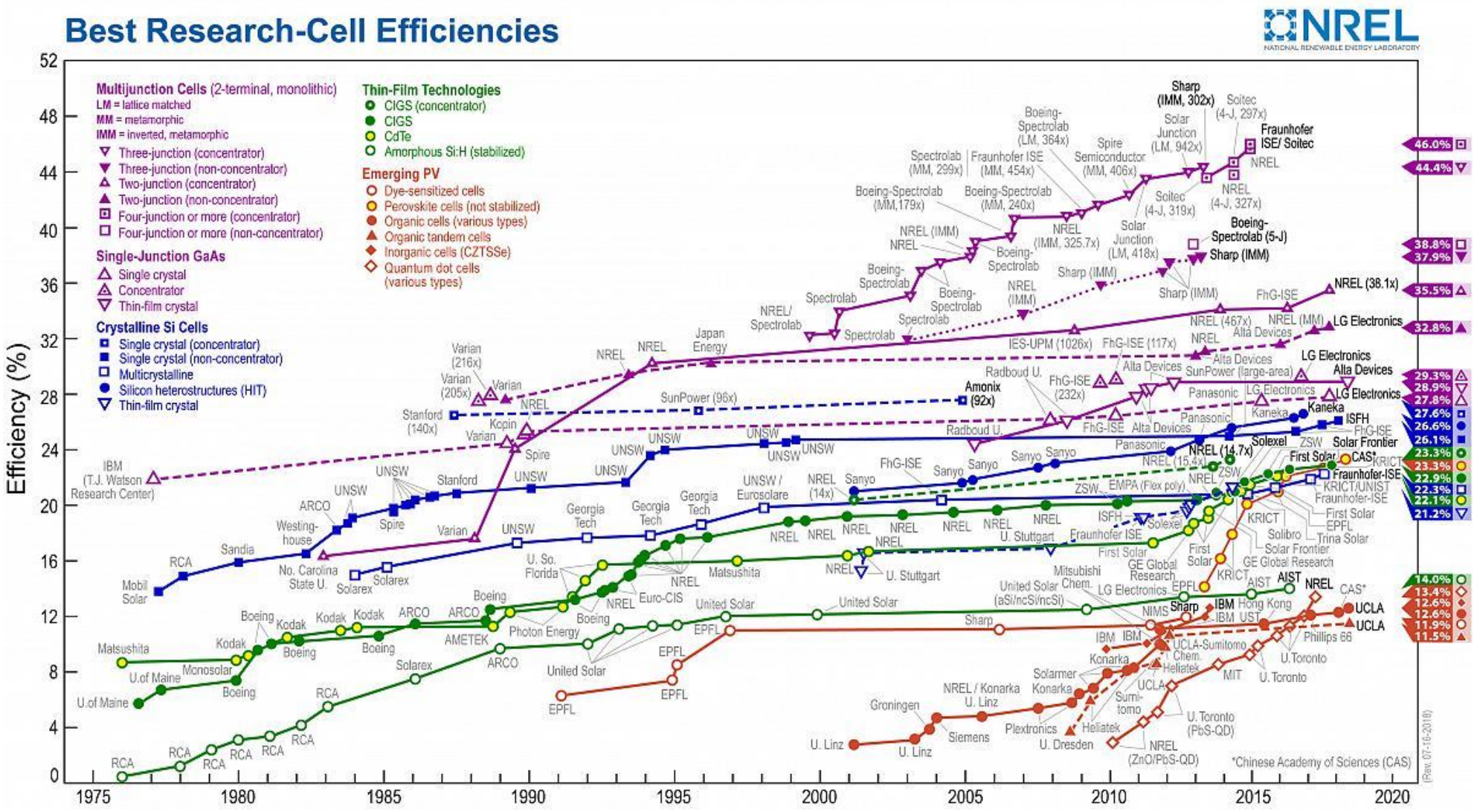

NREL, *Best Research-cell Efficiencies*. 2018.

Appendix 2 Box charts

Photovoltaic performance values for the different configurations of carbon papers and adhesion layers

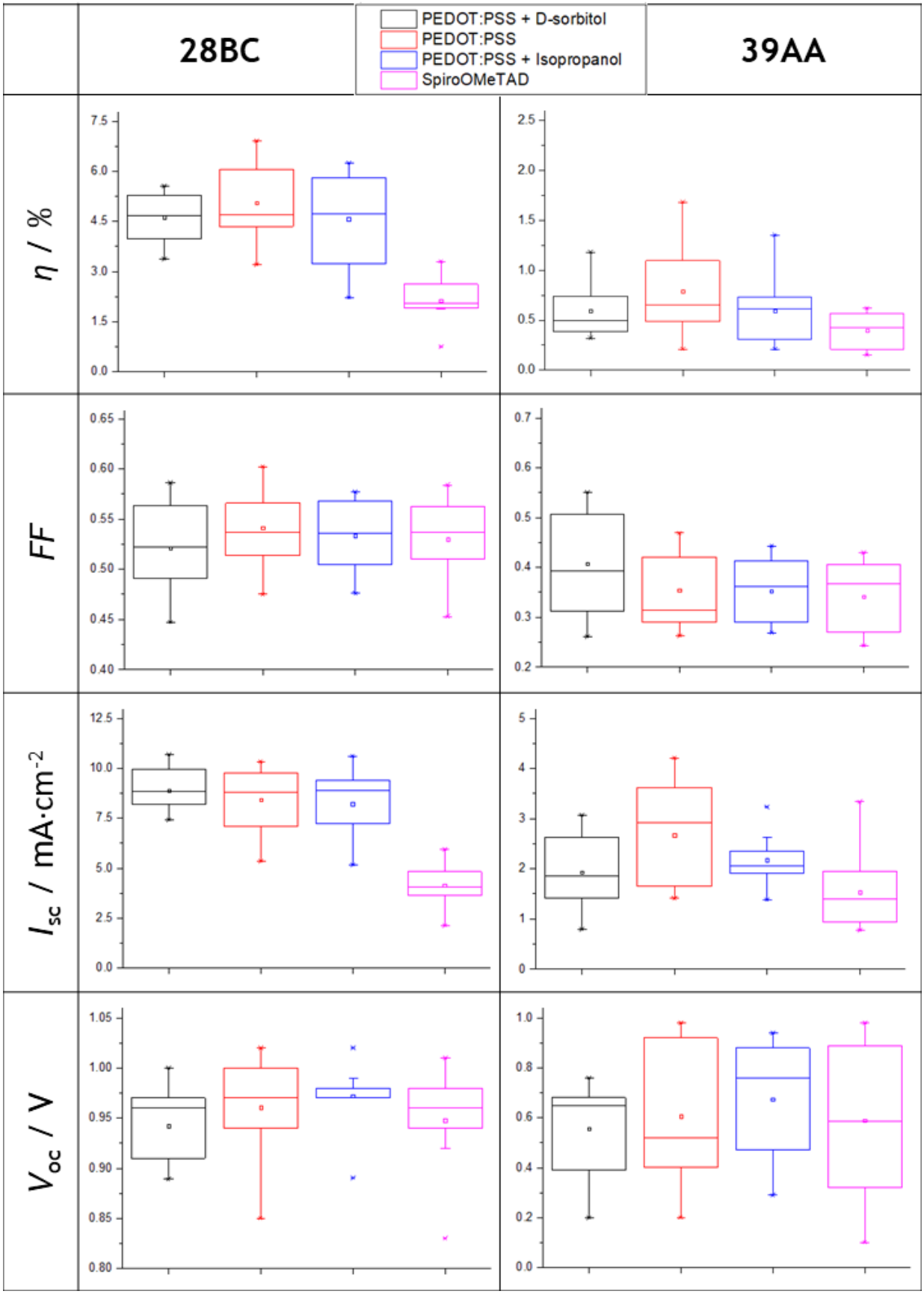

Photovoltaic performance ratios for the different configurations of carbon papers and adhesion layers